ORIGINAL ARTICLE

miR-155 regulates physiological angiogenesis but an miR-155-rich microenvironment disrupts the process by promoting unproductive endothelial sprouting

Yuechao Dong[1] · Florian Alonso[1] · Tiya Jahjah[1] · Isabelle Fremaux[1] · Christophe F. Grosset[2] · Elisabeth Génot[1]

Abstract

Angiogenesis involves cell specification orchestrated by regulatory interactions between the vascular endothelial growth factor and Notch signaling pathways. However, the role of microRNAs in these regulations remains poorly explored. Here we show that a controlled level of miR-155 is essential for proper angiogenesis. In the mouse retina angiogenesis model, antimiR-155 altered neovascularization. In vitro assays established that endogenous miR-155 is involved in podosome formation, activation of the proteolytic machinery and cell migration but not in morphogenesis. The role of miR-155 was explored using miR-155 mimics. In vivo, exposing the developing vasculature to miR-155 promoted hypersprouting, thus phenocopying defects associated with Notch deficiency. Mechanistically, miR-155 overexpression weakened Notch signaling by reducing Smad1/5 expression, leading to the formation of tip cell-like cells which did not reach full invasive capacity and became unable to undergo morphogenesis. These results identify miR-155 as a novel regulator of physiological angiogenesis and as a novel actor of pathological angiogenesis.

Abbreviations

ECs	Endothelial cells
BM	Basement membrane
TNF-α	Tumor necrosis factor α
VEGF-A	Vascular endothelial growth factor A
VEGFR2	Vascular endothelial growth factor receptor 2
Dll4	Delta like Notch ligand 4
NICD	Notch intracellular domain
Jag1	Jagged Notch ligand 1
Nrp1	Neuropilin-1
MMPs	Matrix metalloproteases
miRs	MicroRNAs
HMVECs	Human microvascular ECs
Col-IV	Collagen-IV

Yuechao Dong and Florian Alonso contributed equally.

✉ Elisabeth Génot
   elisabeth.genot@inserm.fr

1   Univ. Bordeaux, INSERM, Centre de Recherche cardio-thoracique de Bordeaux, U1045, 33000 Bordeaux, France

2   Univ. of Bordeaux, INSERM, Biotherapy of Genetic Diseases, Inflammatory Disorders and Cancer, U1035, 33000 Bordeaux, France

Introduction

Angiogenesis is the growth of blood vessels from the existing vasculature. This process is essential during embryonic development but becomes restricted to reproduction and tissue repair during adulthood. Physiological angiogenesis depends on the balance of positive and negative angiogenic modulators within the vascular microenvironment and is short-lived. Within a couple of weeks, the new capillaries become mature microvessels that contain quiescent endothelial cells (ECs) resting on an intact basement membrane (BM). In many chronic diseases, including inflammatory disorders and various cancers, the balance between angiogenic and angiostatic factors is lost, resulting in pathological angiogenesis that persists for much longer periods of time. For example, pathological angiogenesis associated with wound healing may occur after an inflammatory response in which TNF-α production is sustained [1].

At the onset of angiogenesis, ECs degrade the underlying BM, migrate and form sprouts that branch and anastomose. During maturation, ECs rebuild a BM, recruit parenchymal cells, and finally return to quiescence. At the molecular level, initial sprouting is stimulated by proangiogenic factors, commonly vascular endothelial growth factor A

(thereafter VEGF-A), whose binding to VEGFR2 receptor (VEGFR2) upregulates the Notch transmembrane ligand Dll4 and thus the emergence of leading ECs (tip cells) from the established vasculature. Dll4 activates the Notch1 receptor in adjacent cells (stalk cells) to induce proteolytic release of the Notch intracellular domain (NICD) which, in complex with other factors, acts as a transcription factor to mediate the tip cell/stalk cell specification [2–4]. Tip cells have low levels of Notch activity, breach the BM barrier and invade the surrounding stroma, while neighboring stalk cells display high levels of Notch activity, do not sprout but divide to extend the sprout. Stalk cells express another Notch1 ligand, Jag1 [5, 6], which antagonizes Dll4/Notch1 signaling back to the tip cell [5]. In tip cells, the stalk-cell phenotype is actively repressed through neuropilin-1 (Nrp1) expression, which limits the activation of Smad transcription factors in response to Alk1/5 signaling [7, 8].

However, how the selected tip cell acquires its functional characteristics remains incompletely understood. Our recent work highlighted the mechanism by which the explorative tip cell opens the way to enable vessel sprouting [9]. In these cells, the reduction of Notch activity induces the assembly of proteolytic organelles at the plasma membrane, which enable filopodia to break through the BM and dock on the interstitial matrix to allow cell invasion [10]. These structures known as podosomes [11] are actin-based and enriched in metalloproteases (MMPs) [12]. Although podosomes contain proteins of the adhesion machinery, they can be recognized by markers such as cortactin or the scaffolding protein Tks5 that are absent from focal adhesions. While inducing the tip cell phenotype, VEGF-A regulates podosome formation and BM proteolysis is restricted to these sites [9, 11]. Collagen-IV (Col-IV) and laminin are the main components of the BM, but endothelial podosomes selectively degrade Co-IV but not laminin [11]. Col-IV coverage is scarce at podosome areas in tip cells [9]. Vessel remodeling is halted by podosome suppression upon reactivation of the Notch pathway and the BM is restored [9]. VEGF-A and Dll4/Notch1 signaling thus cooperate in a negative feedback loop that specializes endothelial tip and stalk cells to ensure adequate vessel branching and function [3]. However, little is known about the posttranscriptional control of this dynamic process by microRNAs (miRs). miRs are highly conserved, small (~ 22 nucleotides) non-coding RNAs that regulate the expression of dozens of genes at the same time, often coding for proteins involved in the same program, to affect cell physiology in a global manner. These miRs are packaged in extracellular vesicles and exosomes (EVs) that travel through the body and regulate some of their targets remotely. MiR levels are altered in disease conditions and one of the most common disease-related miRs is miR-155 [13, 14]. It is highly upregulated in inflammation and cancer conditions in which increased angiogenesis aggravates the

disease. The endothelium is directly exposed to high levels of miR-155, released by inflammatory cells into the bloodstream, either in complex with argonaute (ago2) or included in EVs [15]. We therefore investigated how this miR affects EC phenotype, function and behavior to explore a possible link between miR-155 gain of function and angiogenesis.

Although some studies have investigated the angiogenic potential of miR-155 in ECs, most of them have used HUVECs and came to conflicting conclusions [16, 17]. Because angiogenic sprouting arises primarily from preexisting microvessels, we addressed the role of miR-155 in the mouse retina model of physiological angiogenesis. Human microvascular ECs (HMVECs) were subsequently used in in vitro assays to unravel step by step the processes that operate in vivo. VEGF-A regulates EC sprouting, cell invasion and migration, and our study established that these processes are dependent on endogenous miR-155. miR-155 participates in podosome formation and associated function, thus regulating EC invasion. However, while stimulating EC sprouting, increasing miR-155 levels impeded cell migration and morphogenesis, thus resulting in unproductive angiogenesis. Thus, balanced expression of miR-155 is required for physiological angiogenesis.

Materials and methods

Mice

Lifeact-EGFP transgenic mice [18] have been previously described. All experimental procedures with mice were performed using protocols approved by the Committee for Ethics of Animal Experiments at the University of Bordeaux, in accordance with the guidelines of the French Ministry of Health under the authority of the project License #18727. Male and female mice were not distinguished. The numbers of analyzed mice are indicated in each experiment.

Intravitreal injections

C57Bl6/J and Lifeact-EGFP transgenic pups at postnatal day 4 (P4) were intravitreally injected with 1 µl of either miR-155 mimics (mmu-miR-155-5p mature sequence UUAAUG CUAAUUGUGAUAGGGGU, miRBase Accession Number MIMAT0000165 or antimiR-155 miRCURY LNA inhibitor (second-generation-specific inhibitor for miR-155, developed by Exiqon) or control miRNA (scrambled oligonucleotides) (all from Qiagen) reconstituted in sterile PBS to a final concentration of 1 µg/µl. MiR-155 and antimiR-155 were injected into the left eye while control miRNA was injected into the contralateral eye at P4. Injections were performed using a 33-gauge needle placed on a 10-µl Nanofil syringe controlled by a UMP3 pump controller (World Precision

Instruments) as previously described [19]. Mice were euthanized 2 days later (P6) and their eyes were collected and fixed to analyze flat-mount retinas.

Whole retina immunohistochemistry

Eyes were fixed in 4% paraformaldehyde for 2 h at 4 °C. Retinas were dissected, then incubated for 2 h at room temperature in blocking buffer (PBS, 2% BSA, 0.2% Triton X-100). After three 20 min washes in Pblec buffer (PBS supplemented with 1 mM $MgCl_2$, 1 mM $MnCl_2$, 1 mM $CaCl_2$ and 1% Triton X-100), retinas were incubated overnight at 4 °C with fluorescein-labeled isolectin B4 (IB4; Vector Laboratories, FL-1201, 1:25) or rhodamine-labeled IB4 (IB4; Vector Laboratories, RL-1102, 1:25) and antibodies diluted in blocking buffer. Retinas were washed three times with blocking buffer and incubated with species-specific fluorescent-labeled secondary antibodies (Jackson Laboratories, 1:100) diluted in blocking buffer for 2 h at room temperature. After three washes in PBS, whole retinas were flat-mounted in ProLong Gold Antifade reagent (Life Technologies) containing Hoechst 33342 (Life Technologies), and analyzed with an epifluorescence microscope (Nikon TE-2000) or a laser scanning fluorescence microscope (Zeiss LSM 510 Meta inverted).

Antibodies for immunolabeling

Antibodies against cortactin (clone 4F11, #05-180) were obtained from Millipore. Col-IV antibodies were obtained from BioRad (#2150-1470). Antibodies against VE-Cadherin (clone 11D4.1, #555289) were obtained from BD Pharmingen. Antibodies against serum albumin (AF3329) were purchased from Biotechne. Antibodies against phospho-SMAD1/5/8 (#13820) were from Cell Signaling Technologies. Antibodies against ERG 1/2/3 (ab92513) were from Abcam. For secondary detection, species-specific fluorescent-labeled secondary antibodies (Jackson ImmunoResearch) were used.

Analysis of neonatal retinal vasculature

To quantify vascular progression within neonatal retinas, mosaic images of IB4-labeled retinas were obtained by stitching individual images acquired at 4 × magnification with a fluorescence microscope (Nikon TE-2000) using the 'large image' function of the NIS-elements software. From these pictures, the vascular coverage (IB4-positive retina area normalized to the total retina area), the radial extension of the vessels (distance from the optic nerve to the extremity of the network; measured in each quarter of the retinas), and the vascular density at the angiogenic front (percentage of IB4-positive areas per field, determined in ROIs from each quarter of the retinas) were quantified using the ImageJ software [20], as previously published [9]. The number of sprouts and tip cells per ROI at angiogenic fronts was determined by manual counting. To quantify podosome number, average podosome size and Col-IV coverage at angiogenic fronts, z-stack confocal series of 20 optical sections ($x/y/z = 146.25 \times 146.25 \times 0.15$ μm) were acquired with a 63 × oil immersion objective. Acquisitions were performed at the leading front of the developing retinal vasculature. To determine the density of podosomes per μm^2 of EC, the mean number and size of podosomes (F-actin/cortactin-positive (yellow) foci) per vessel length were calculated using the ImageJ "Analyze Particles" function performed on maximal intensity projections of the confocal stacks after deconvolution (AutoQuant X3 software) and normalization to the Lifeact-EGFP-positive surface area (determined from the thresholded image of the corresponding channel). To determine Col-IV coverage of retinal vessels, the Col-IV-positive surface area per field was determined on thresholded images and normalized to the Lifeact-EGFP-positive surface area, as previously described [9]. The number of filopodia and empty sleeves per ROI at angiogenic fronts was determined by manual counting and normalized respectively by the number of tip cells and the IB4 positive surface area. To determine VE-Cadherin and P-Smad1/5/8 expression at angiogenic front, the VE-Cadherin-positive surface area per field and the number of P-Smad1/5/8 and IB4 double positive cells were determined on thresholded images and normalized to the IB4-positive surface area. To determine albumin extravasation at remodeling plexus, the albumin-positive surface areas per field that were negative for IB4 were measured on thresholded images.

Cells, cell culture and cell stimulation

In most experiments, Human Pulmonary Microvascular Endothelial cells (HMVECs, Cell Systems, #ACBRI 468 V) were used. HMVECs were maintained in complete EC growth medium (EGM-MV; Promocell, a culture medium that does not contain VEGF) containing antibiotics at 37 °C in a 5% CO_2 humidified atmosphere and used between passages 2 and 7. Cells were trypsinized and seeded in complete medium at 0.5×10^6 cells per well in six-well plates for western blot experiments and RT-qPCR experiments, and at 1.5×10^4 cells on glass coverslips in four-well plates for immunofluorescence imaging. For stimulation, human recombinant VEGF-A (used at 25 ng/ml in all experiments, unless otherwise indicated) was obtained from Promocell and human recombinant TNF-α (used at 5 ng/ml) were obtained from Biotechne. For pharmacological inhibition of Notch signaling, the γ-secretase inhibitor DAPT (used at 10 μM) was obtained from Sigma. HUVEC, BAEC and HAOEC cells were cultured as previously described [21, 22].

Tumor cell lines were cultured as reported: AGS, HeLa and JEG-3 cells in αMEM medium; HTR-8/SVneo and JEG-3 cells in DMEM/F12 medium, BeWo cells in F-12K medium, Jurkat, HCL-7876 and Eskol cells in RPMI-1640 medium, from Thermofisher. The MCF10A cell line was grown in MEBM™ Basal Medium (CC-3151) and MEGM™ Single-Quots™ Supplements (CC-4136) obtained from Lonza. All media were supplemented with 10% FCS, L-glutamine and antibiotics (Thermofisher). HuH-7 and MDA-MB-231 cells were grown as previously described [23].

Cell transfection with siRNAs, miR-155 mimic or antimiR-155

Transfection of HMVECs was performed by two rounds of transfection, 24 h apart, with double-stranded short interfering RNA (siRNA), siRNA MT1-MMP (MMP-14 #L-004145), siRNA Smad1 (5′-AACACTGGTGCTCTA TTGTCT-3′) and siRNA Smad5 (5′-AAAGCCTTGAGC AGTCCAGGA-3′) [24]. miR-155 mimic (miRIDIAN microRNA Human hsa-miR-155-5p-mimic) or antimiR-155 (miRIDIAN microRNA hsa-miR-155-5p hairpin inhibitor against miR-155, synthesized by Dharmacon [25]) at 20 nM using a calcium phosphate precipitation protocol [26]. On the next day, cells were replated, cultured for 1 day and then used in the various assays.

qRT-PCR analysis of messenger RNA expression

Cells were homogenized in Trizol reagent and total RNA was extracted using the RNeasy kit (Qiagen) following the manufacturer's procedure. Transcripts (1 µg) were reverse-transcribed using High Capacity cDNA Reverse Transcription (Thermofisher). Quantitative PCR was performed using the 2 × Takyon for Syber Assay (Eurogentec) in a MX3000P from Stratagene. cDNAs were amplified using the following primers: human GAPDH: GAAGGTGAAGGTCGGAGTC (forward) and GAAGATGGTGATGGGATTTC (reverse); VEGF-A forward: CCTTGCCTTGCTGCTCTAC, reverse: TTCTGCCCTCCTCCTTCTG; VEGF-B forward: GGA CAGAGTTGGAAGAGGAGAC (reverse): GGAAGAGCC AGTTGTAAGATGC; VEGF-C forward: CAGACAAGT TCAT TCCAT TAT TAG, reverse: AGTCATCTCCAG C ATCCG; VEGF-D forward: TCCAGACCAACCTTC CATTCAC, reverse: CAGCACACCTTTCTCATTCACC. 'siRNA' refers to mRNA obtained from siRNA transfected cells and 'control' refers to control siRNA transfected cells.

The mRNA levels were normalized to the levels of housekeeping genes and the fold change was calculated using the following formula: $2^{-\Delta\Delta Ct} = 2^{-\{(Ct,TG-Ct,CG)_{miRNA} - (Ct,TG-Ct,CG)_{control}\}}$ where Ct, TG represents the crossing threshold for the target gene and Ct, CG represents the crossing threshold for the housekeeping gene.

qRT-PCR assessment of miR-155 expression

Total RNA was extracted from cells homogenized in Trizol reagent (Thermofisher) using the Qiagen miRNeasy kit. Transcripts (10 ng) were reverse-transcribed using the miR-CURY LNA RT kit from Qiagen. Quantitative PCR was performed using the miRCURY LNA SYBR green kit from Qiagen in a MX3000P from Stratagene. miR-155 was quantified using specific primers from Qiagen: miRCURY LNA miRNA PCR Assays YP00204308. Absolute quantification of miR155 was performed using a miR-155 mimics standard curve and reported to 10 ng of RNA used as a template for reverse transcription.

In situ matrix degradation assay

For the gelatin degradation assay, glass coverslips were first coated with Oregon-green-488 gelatin diluted to 0.1% in PBS at RT for 30 min, washed with PBS and fixed with 0.5% glutaraldehyde (EMS) for 15 min. After washing with PBS, coverslips were incubated in 5 mg/ml sodium borohydride for 30 min under constant agitation, washed three times in PBS and finally incubated with culture medium before adding the cells. After adhesion, cells were treated or not with VEGF-A for 24 h, then fixed and processed for immunofluorescence staining. Quantification of degradation areas on fluorescence-labeled matrices was performed for at least ten fields (Å ~ 10 × objective lens) for each coverslip. The areas of degradation were quantified using ImageJ software as described in [27]. Briefly, black and white images of gelatin degradation were analyzed by manually adjusting the threshold on each picture until the selected areas were representative of the real degradation observed in the original color image. Then, the total loss of matrix-based fluorescence per field was measured by the Analyze Particles function. The total degradation area (expressed in μm^2) was then normalized for the number of cells (degradation index). Control values were arbitrarily taken as 1.

In vitro tube formation assay on Matrigel

In vitro tube formation assays were performed in a pre-chilled 96-well plate with 70 µl per well of growth factor-reduced Matrigel (a BM-like material derived from Engelbreth–Holm–Swarm tumor cells, purchased from Corning) that was allowed to gel at 37 °C for 15 min. Thereafter, 1×10^4 HMVECs were seeded in triplicate onto the Matrigel in EGM-MV complete media containing VEGF-A, incubated at 37 °C for 18 h to allow formation of tubular structures and further analyzed by microscopy using a Nikon Eclipse TE2000-E (Nikon Ltd) at 4 × magnification. The angiogenic response was measured by image analysis.

Quantification of capillary-like structures was performed using the Angiogenesis analyzer plug-in on ImageJ software.

Wound healing assay

To investigate cell migration, ECs (2×10^5) were seeded in 12-well plates and then cultured in complete medium for 2 days until confluence. The confluent layers of ECs were carefully scratched using a pipette yellow tip (100-µl volume) to create an artificial wound. The wells were then washed twice with PBS to remove cell debris and cultured for 24 h. Phase contrast images were taken at different time intervals (0, 4 h, 8 h, and 24 h) to monitor repopulation in the scratched area. The acellular area measured at each time point was calculated with ImageJ.

Angiogenesis invasion assay (AIA)

A cut yellow tip was placed centrally in a 3.5 cm MatTek dish (MatTek Corporation, USA) and filled with pure growth-factor-reduced Matrigel™ (67 µl at around 9 mg/ml) plus VEGF-A (3 µl) to create a BM-like matrix barrier, as previously described [9]. Matrigel plugs were then allowed to polymerize for 30 min in the incubator at 37 °C, 5% CO_2. After this step, the yellow pipette tip was carefully removed. Cells (5×10^4) were seeded around the Matrigel plot and allowed to adhere for 2 h at 37 °C and 2 ml of complete medium were then layered on top. The dish was returned to 37 °C for 12 h. Then cells in AIA were fixed in 2% PFA for 30 min, followed by quenching with 50 mM NH_4Cl and permeabilization in 0.2% Triton X-100 for 1 h and blocking in 3% BSA. Primary monoclonal antibodies against cortactin were used at a 1/100 dilution in blocking buffer. After 16 h at 4 °C, cells were washed extensively in PBS, then an Alexa fluor-546 coupled secondary antibody against mouse IgG (Jackson ImmunoResearch) was added at 1/100 dilution in blocking buffer together with Alexa fluor-488 labeled phalloidin (Thermofisher Scientific) and Hoechst 33342 (Life Technologies) for 3 h at room temperature. The system was then mounted with anti-fade reagent (Life Technologies). To quantify the number of sprouts invading the Matrigel plug, mosaic images were obtained by stitching individual phase-contrast images acquired at 4× magnification with an automated microscope (Nikon TE-2000) using the 'large image' function of the NIS-elements software. On the obtained images, the number of sprouts was determined manually and the length of individual sprouts was measured using the "straight line" tool of ImageJ, from the tip to the root of sprouts. From these measurements, the mean sprout length and the sum of sprout lengths were determined by averaging and summing the values obtained for all individual sprout lengths, respectively. To compare the different experiments/conditions, the number of sprouts and the sum of the sprout lengths were normalized by the length of the cell monolayer-Matrigel interface used to perform the measurements.

To quantify podosome number and average podosome size in ECs, z-stack confocal series of 10 optical sections ($x/y/z = 146.25 \times 146.25 \times 0.15$ µm) were acquired using a laser scanning fluorescence microscope (Zeiss LSM 510 Meta inverted) equipped with a 63× oil immersion objective. The mean number of podosomes (F-actin/cortactin-positive (yellow) foci) per sprout was calculated using the ImageJ "Analyze Particles" function performed on maximal intensity projections of the confocal stacks. The mean number of podosomes was normalized to the cellular area.

Indirect immunofluorescence

Sub-confluent cells grown on glass coverslips were fixed for 30 min at room temperature in 4% (w/v) paraformaldehyde containing PBS, permeabilized for 15 min at room temperature with 0.1% Triton X-100 containing PBS, blocked for 30 min at room temperature in 3% BSA containing PBS and incubated for 1 h at room temperature with primary antibodies diluted at 1/100 in blocking buffer. Antibodies against Cortactin (#sc-11408) were from Santa Cruz. Antibodies against Vinculin (#V9131) were from Sigma. Antibodies against Paxillin (#04-581) were from Millipore. Antibodies against VE-Cadherin (#BMS158) were from eBioscience. F-actin was visualized with Alexa Fluor 647-labelled phalloidin (Thermofisher Scientific) and the nuclei were stained with Hoechst 33342 together with fluorescent secondary antibodies (Jackson ImmunoResearch) for 1 h at room temperature. The coverslips were washed in water and mounted on microscope slides with ProLong Gold Antifade reagent (Life Technologies). For MT1-MMP cell surface exposure, the permeabilization step was omitted and cells were incubated for 1 h with MT1-MMP antibodies (Abcam, Ab51074) after several PBS washes. Another 30-min step with 4% PFA was performed to fix the antibodies before permeabilizing with 0.1% Triton X-100 and immunofluorescent staining as above. When assessing podosome formation, for each structure found, its location at the base of the cell was systemically checked to confirm that it was not a dorsal ruffle. The number and area of focal adhesions in ECs were determined using the "Analyze Particles" function of ImageJ performed on thresholded images. The number of focal adhesions was normalized to the cellular area to obtain the value of focal adhesion density.

Western blot analysis

Cells were transfected with siRNA as indicated. On the next day, cells were stimulated with 25 ng/ml VEGF-A (Promocell) for 24 h then lysed for immunoblotting. Lysis was performed directly in Laemmli sample buffer and samples

were run on a 10% SDS-PAGE gel at 120 V for 90 min. Proteins were transferred onto Immobilon polyvinylidene difluoride membranes (Merck Millipore) at 120 V for 1 h. Membranes were saturated with 5% bovine serum albumin in Tris-buffered saline containing 0.1% Tween-20 for 1 h and incubated overnight at 4 °C with primary antibodies. Antibodies against Dll4 (#2589), Jag1 (#70109), Smad1 (#9743), Nrp1 (#3725), α-actinin (#6487), P-Smad1/5/8 (#9511) and NICD (#4147) were from Cell Signaling Technologies. Other antibodies were Smad5 (Abcam #Ab40771) and α-tubulin (Sigma, clone DM1A, #T9026). Then, primary antibodies were revealed using horseradish peroxidase-coupled anti-mouse, anti-goat or anti-rabbit (Jackson ImmunoResearch) secondary antibodies for 1 h. Finally, horseradish peroxidase activity was revealed using a chemiluminescence kit (GE-healthcare) according to the manufacturer's instructions. Auto-radiographies were digitized and band intensities were quantified using NIH ImageJ. Protein expression was normalized against tubulin and made relative to the control (i.e., siRNA Smad1/siRNA control condition) for representation on graphs.

Analysis of matrix metalloproteinases activity by zymography

HMVEC transfected with control, miR-155 or anti-miR155 were seeded at 150,000 cells per well in 6-well plates and then stimulated with VEGF-A for 24 h. MMP activity was measured in cell supernatants. Gelatinolytic activity was assayed by SDS PAGE, in 10% polyacrylamide gels containing 1 mg/ml gelatin as described [28]. For secreted MMPs, Samples were obtained by mixing 175 μl of supernatants with 35 μl 6 × sample buffer (300 mM Tris–HCl, 12% SDS, 0.1% bromophenol blue, 60% glycerol, pH 6.8). Gels were then incubated in 2.5% Triton X-100 for 60 min to remove SDS followed by overnight incubation in developing buffer (50 mM Tris–HCl, 0.2 M NaCl, 5 mM CaCl$_2$, 0.02%Brij-35 pH 7.6). Gels were stained for 30 min in 30% methanol, 10% glacial acetic acid, 0.5% Coomassie Blue G-250, then destained for 1 h in 30% methanol, 10% glacial acetic acid. Gels were digitized and band intensity was quantified using NIH ImageJ.

Statistics

Statistical analysis was performed with GraphPad Prism 6 (GraphPad Software, Inc., San Diego. CA, USA). Data represent at least three independent experiments. Graphs are presented as mean values ± SD or SEM (bars). For experiments involving animals, individual values (dots) (scatter plot with bar) were added. Significance was determined using Student's *t* test or the one-way or two-way ANOVA, followed by Tukey's or Bonferroni's post-tests, whichever

applicable. p values < 0.05 were considered statistically significant.

Results

Exposure of vasculature to either miR-155 or anti-miR-155 disrupts physiological angiogenesis

To address the role of miR-155 in sprouting angiogenesis, we used the mouse postnatal retina model that allows simultaneous visualization of the different steps of the angiogenic process [29]. In the first week after birth, a primary vascular plexus grows from the optic nerve head of the retina. Guided by fibronectin produced by proangiogenic astrocytes and exposed to a VEGF-A gradient, the vascular network develops radially toward the periphery of the retina. Angiogenesis can be monitored by multi-parametric characterization of this 2D plexus growing onto the retinal surface between P0 and P8. We performed intravitreal injection of either miR-155 mimics (a fluorescent tagged synthetic oligonucleotide corresponding to endogenous mature miR-155) or its antagonist (antimiR-155, a fluorescent tagged synthetic oligonucleotide neutralizing endogenous miR-155) in the eye at P4 and allowed neo-vascularization until P6 (Fig. 1a). FAM fluorescence in flat-mounted P6 retinas confirmed that the oligonucleotides were taken up by the cells (Fig. 1b). Analysis of the angiogenic front in P6 retinas stained for the endothelial marker isolectin B4 (IB4) revealed that the density of capillaries and the number of sprouts were increased in miR-155-injected eyes as compared to controls (Fig. 1c, d). The vascular coverage of the retina and the radial extension of the network were not significantly affected. Further analysis revealed no alteration in filopodial protrusions, empty sleeves (Col-IV staining) or endothelial cell–cell junctions (VE cadherin staining) in eyes injected with miR-155 (Fig. S1a, b). In contrast, all angiogenic parameters were affected in antimiR-155-injected eyes as compared to controls (Fig. 1c, d and Fig. S1a, b) indicating that endogenous miR-155 is required for developmental angiogenesis. We did not detect arteriovenous malformation in the injected retinas.

Sprouting tip cells use podosomes to breach the BM surrounding the parental vessel [9]. Alterations in the sprouting, branching and anastomosing capacities of retinal vessels in miR-155- or anti-miR-155-injected eyes could therefore reflect changes in the ability of tip cells to assemble these structures. To study podosome formation, we used Lifeact-EGFP-transgenic mice [18] in which the expression of the transgene is largely restricted to the endothelium [30]. Podosomes are detected by the colocalization of F-actin and cortactin staining in punctate structures that coincide with gaps in the Col-IV labeling at the distal end of tip cells where filipodia extend from the leading edge [9]. In
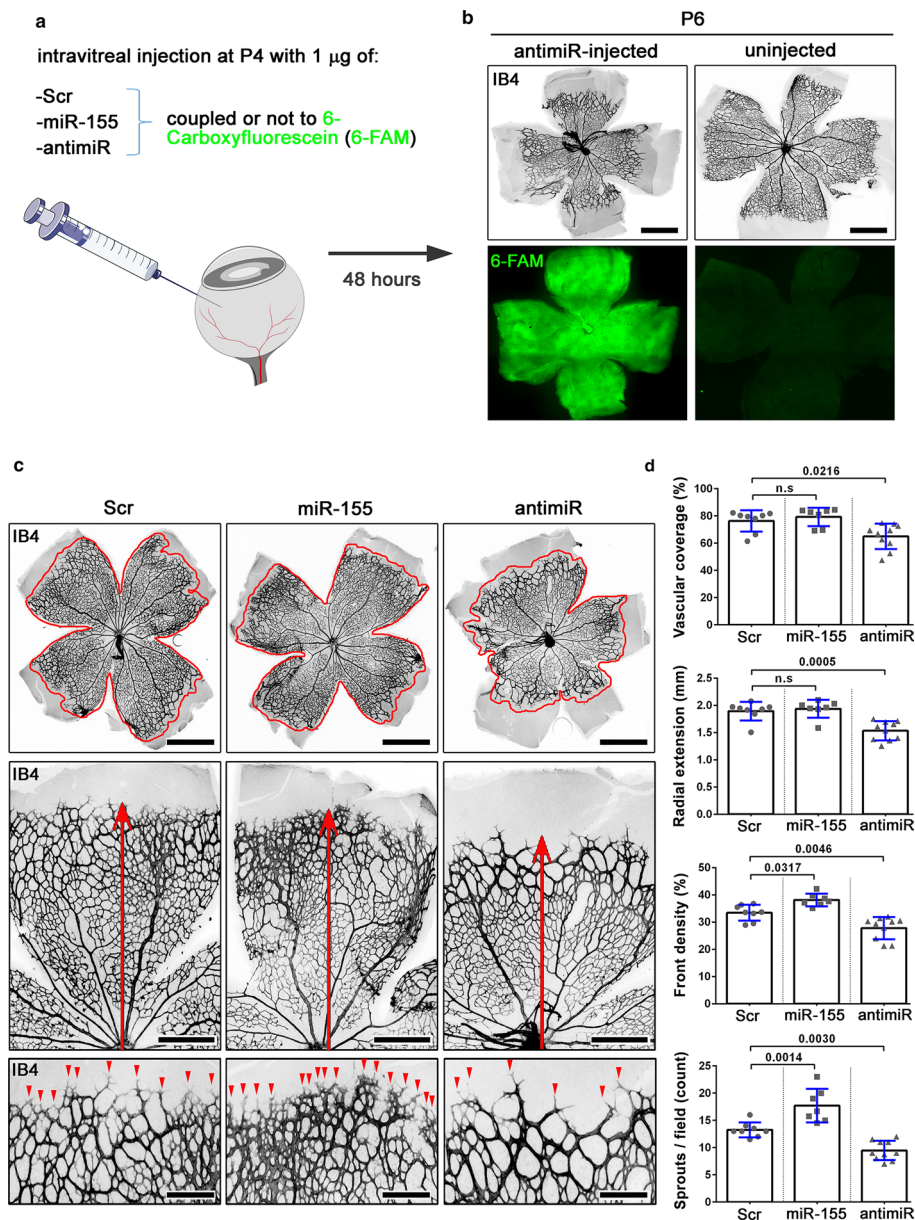
Fig. 1 Exposure of developing vasculature to either miR-155 or anti-miR-155 disrupts physiological retinal angiogenesis. **a** Schematic representation of the protocol of intravitreal administration of oligonucleotides. 4-day-old C57Bl6/J animals are intravitreally injected with 1 µg of either miR-155, antimir-155 and a scrambled version of miR-155 oligonucleotides conjugated or not with 6-carboxyfluorescein (6-FAM). **b** 48 h after injections, P6 mice are sacrificed and retinas are dissected. Then, retinas are subjected to whole mount immunohistochemistry. Labeling of retinas for the endothelial marker IB4 (black) reveals the developing vascular network. 6-FAM fluorescence (green) is also detected in oligonucleotide-injected eyes (left panels) while no signal is detected in those from non-injected ones (right panels). Scale bars: 1 mm. **c** IB4 (black) stained retinal wholemounts from P6 mice intravitreally injected with the scrambled (Scr), miR-155 or antimiR-155 oligonucleotides at P4. **d** Quantifications and representative images of the vascular coverage (delimited by red line, top panels), radial extension (red arrow, middle panels), capillary density and sprouting (red arrowheads bottom panels) are shown ($n=8$ Scr-injected; $n=7$ miR-155-injected; $n=9$ antimiR-155-in-

jected mice). Graphs are presented as mean values $\pm$ SD (bars) and individual values (dots). A p-value less than 0.05 was considered as statistically significant (one-way ANOVA followed by Tukey's post-test). Scale bars: 1 mm (top panels), 200 µm (middle panels) and 100 µm (right panels). **e** Representative images of the vascular front of Lifeact-EGFP P6 animals intravitreally injected with Scr-, miR-155- and antimiR-155-oligonucleotides at P4. Retinas are labeled for F-actin (Lifeact-EGFP, green), cortactin (red) and Col-IV (Col-IV, white). Scale bars: 20 µm. **f** High magnification images from the three regions boxed in **e**. Tip cell podosomes are highlighted by F-actin and cortactin staining (yellow foci) in areas devoid of Col-IV staining. Scale bars: 5 µm. **g** Quantitative analyses of podosome density, podosome area and coverage of the neovessels with Col-IV are shown ($n=7$ Scr-injected; $n=8$ miR-155-injected; $n=6$ antimiR-155-injected Lifeact-EGFP mice). Graphs are presented as mean values $\pm$ SD (bars) and individual values (dots). A p value less than 0.05 was considered as statistically significant (one-way ANOVA followed by Tukey's post-test)
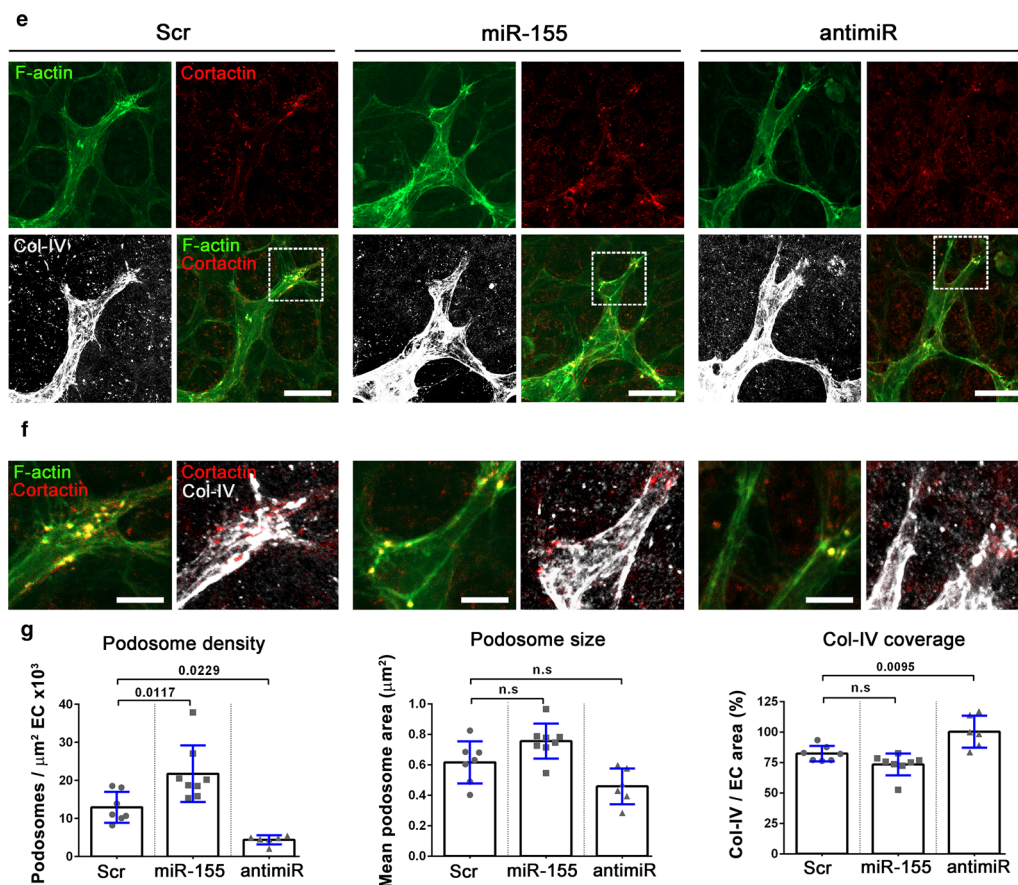
Fig. 1 (continued)

miR-155-injected eyes, the number of podosomes per tip cell was increased, whereas fewer podosomes were formed in tip cells from antimiR-155-injected eyes than in controls (Fig. 1e–g). Jointly, the overall Col-IV coverage of tip cells tended to decrease in miR-155-injected eyes while it was significantly increased in antimiR-155-injected eyes (Fig. 1g). These differences may be related to modulation of podosome formation and activity by miR-155 and antimiR-155, but could also reflect modulation of Col-IV synthesis. Neither miR-155 nor antimiR-155 altered podosome size, indirectly indicating that miR-155 did not affect actin dynamics in podosomes (Fig. 1g).

Collectively, these results show that miR-155 is essential for proper angiogenesis in vivo. However, a miR-155-rich microenvironment affects neo-vascularization. miR-155 promotes vascular sprouting and podosome formation in tip cells, while antimiR155 has the opposite effect. Interestingly, aberrant sprouting and exacerbated podosome formation are hallmarks of impaired Notch signaling, as seen in vessels exposed to DAPT (a γ-secretase inhibitor) [9]. The miR-155 phenotype is therefore reminiscent of one in which Notch signaling is inhibited.

Increased miR-155 levels in endothelial cells alter their ability to migrate, sprout and undergo morphogenesis

To explore the cellular mechanisms underlying the disruptive effect of miR-155 on retinal angiogenesis, we altered miR-155 levels in microvascular ECs (HMVECs) and addressed their functional properties and behavior in vitro. qRT-PCR experiments confirmed that HMVECs express miR-155 (Fig. S2a). Its level was not modulated by cell confluence (Fig. S2b) and was found slightly higher than that of arterial ECs (Fig. S2c). Importantly, VEGF-A did not alter miR-155 expression (TNF-α was effective as expected) (Fig. S2d) and miR-155 did not regulate VEGF expression (Fig. S2e). We used an in vitro angiogenesis assay (AIA) that we have developed to examine how miR-155 affects tip cell/stalk cell specification [9]. It simulates the initial sprouting phase of angiogenesis in which ECs differentiate into invasive tip cells that assemble proteolytic podosomes to breach the BM [9]. To this end, a Matrigel plug (a BM-like material) supplemented with VEGF-A was placed in a culture dish and HMVECs were seeded to form a monolayer around it (Fig. 2a, b). Tip cell-like cells differentiating from

ECs at the Matrigel interface assembled podosomes, projected filopodia toward the VEGF-A source, and sprouted into the Matrigel plug (Fig. 2b, c). When transfected with miR-155 mimics, ECs sprouted in the Matrigel at higher frequency than control ECs. However, many sprouts failed to elongate toward the VEGF-A source and remained round in shape (hereafter referred to as immature sprouts) (Fig. 2c–e). Thus, despite increased sprouting, miR-155 did not promote an overall increase in sprout length (Fig. 2e, f). The defect was not due to altered podosome formation: on the contrary, more podosomes per sprout were scored in miR-155 transfected ECs than in controls (Fig. 2g–j). In addition, increasing the VEGF-A concentration in the Matrigel plug did not overcome the inhibitory effect of miR-155 on EC invasion. qRT-PCR experiments confirmed that Matrigel did not significantly affect miR-155 levels in HMVECs (Fig. S2f). Conversely, and similar to the in vivo situation, antimiR-155 transfection reduced EC sprouting and podosome formation below baseline (Fig. 2d, g–j), resulting in an overall reduction in sprout length (Fig. 2f).

To determine whether the reduced invading capacity of miR-155-transfected cells could result from a defect in VEGF-A-induced chemotaxis, we assessed their migration potential directly in the wound-healing assay. Whereas VEGF-A stimulation allowed control cells to fill the gap within 24 h, cells over-expressing miR-155 did not (Fig. 3a, b). miR-155- and antimiR-155-transfected cells were less motile than control cells. Neutralization of endogenous miR-155 with the antimiR-155 slowed down cell migration but this defect was partially rescued by VEGF-A. Cell proliferation was not affected in miR-155 or antimiR-155 transfected cells. Immunofluorescent staining for F-actin and the scaffolding protein paxillin were used to examine focal adhesions (Fig. S3a). miR-155-transfected cells did not exhibit detectable morphological changes or alterations in stress fiber organization but defects in cell–matrix adhesion (Fig. 3c–f, Fig. S3b). Whereas VEGF-A increased the number of focal adhesions per cell in control ECs, this response did not occur in miR-155-transfected cells. VEGF-A or antimiR-155 did not affect the overall area of focal adhesions (Fig. 3d). In contrast, miR-155 over-expression increased the mean size of focal adhesions (Fig. 3e), suggesting an alteration in their turnover that could account for the migration defect [31].

ECs undergo morphogenesis in the late steps of angiogenesis, a process that can be simulated in vitro by plating cells on BM-like materials [32] (Fig. 4a). Typically, Matrigel evokes capillary-like formation within 24 h. ECs first align themselves end-to-end, then elongate, and a complex network of anastomosing cells can be observed after 16 h. While the typical capillary-like structures were observed in control HMVECs, miR-155-enriched cells tended to aggregate rather than align and elongate (Fig. 4b,

c). Tubulogenesis was unaffected for cells transfected with antimiR-155 (Fig. 4b, c).

Collectively, these results show that the phenotypes and properties of ECs over-expressing or under-expressing miR-155 analyzed in the AIA mirror the in vivo situation in which the retinal vasculature is exposed to miR-155 or antimiR-155, respectively. Endogenous miR-155 plays a decisive role in podosome formation and cell migration but is not required for morphogenesis. If miR-155 is over-expressed, cell sprouting is stimulated but cell invasion does not occur, as the response to VEGF-A adhesive and migratory signals is impaired. The opposite effects of miR-155 and antimiR-155 on morphogenesis suggest that miR-155 could be turned off at this stage.

miR-155 promotes a proteolytic phenotype

To explore how miR-155 regulates EC sprouting capacities, we examined the ability of HMVECs to assemble functional podosomes in response to miR-155 modulating signals, in the absence of BM cues. HMVECs were transfected with miR-155 mimics or antimiR-155, seeded on a gelatin matrix and stimulated or not with VEGF-A. In 2D cultures, podosomes appear as F-actin-rich cores, each surrounded by an adhesive ring structure containing proteins that are also found in focal adhesions. Nevertheless, podosome are clearly distinguishable from focal adhesions. They can be identified using the F-actin-cortactin double staining and their organization into cluster-like cytoskeletal superstructures often termed podosome rosettes at the ventral membrane of the cell [12] (Fig. S3a, b). In this setting, increasing miR-155 levels promoted podosome rosette formation in HMVECs (Fig. 5a, b). The rosettes featured characteristics similar to those formed in response to VEGF-A and the magnitude of the response was similar [11]. In addition, miR-155 and VEGF-A did not show any additive or synergistic effect (Fig. 5a, b). The miR-155 stimulatory effect was also observed for cells seeded on BM matrix proteins (Col-IV, laminin or Matrigel), but not on the interstitial protein fibronectin or Collagen-I (Col-I) (Fig. S4). By contrast, antimiR-155 decreased the formation of spontaneous podosomes that form at low levels under basal conditions [11] (Fig. 5b). Here again, antimiR-155 suppressed podosome formation in response to VEGF-A, further confirming the need for endogenous miR-155 in this process. The podosome response is reflected in matrix proteolysis that we measured in situ by quantifying dark areas in fluorescent gelatin (Fig. 5c, d). Consistent with the podosome response, miR-155-induced matrix degrading activity was not stimulated further in the presence of VEGF-A. Of note, matrix degradation may have been slightly underestimated under these conditions because motility was affected in miR-155-transfected cells (Fig. 3b).
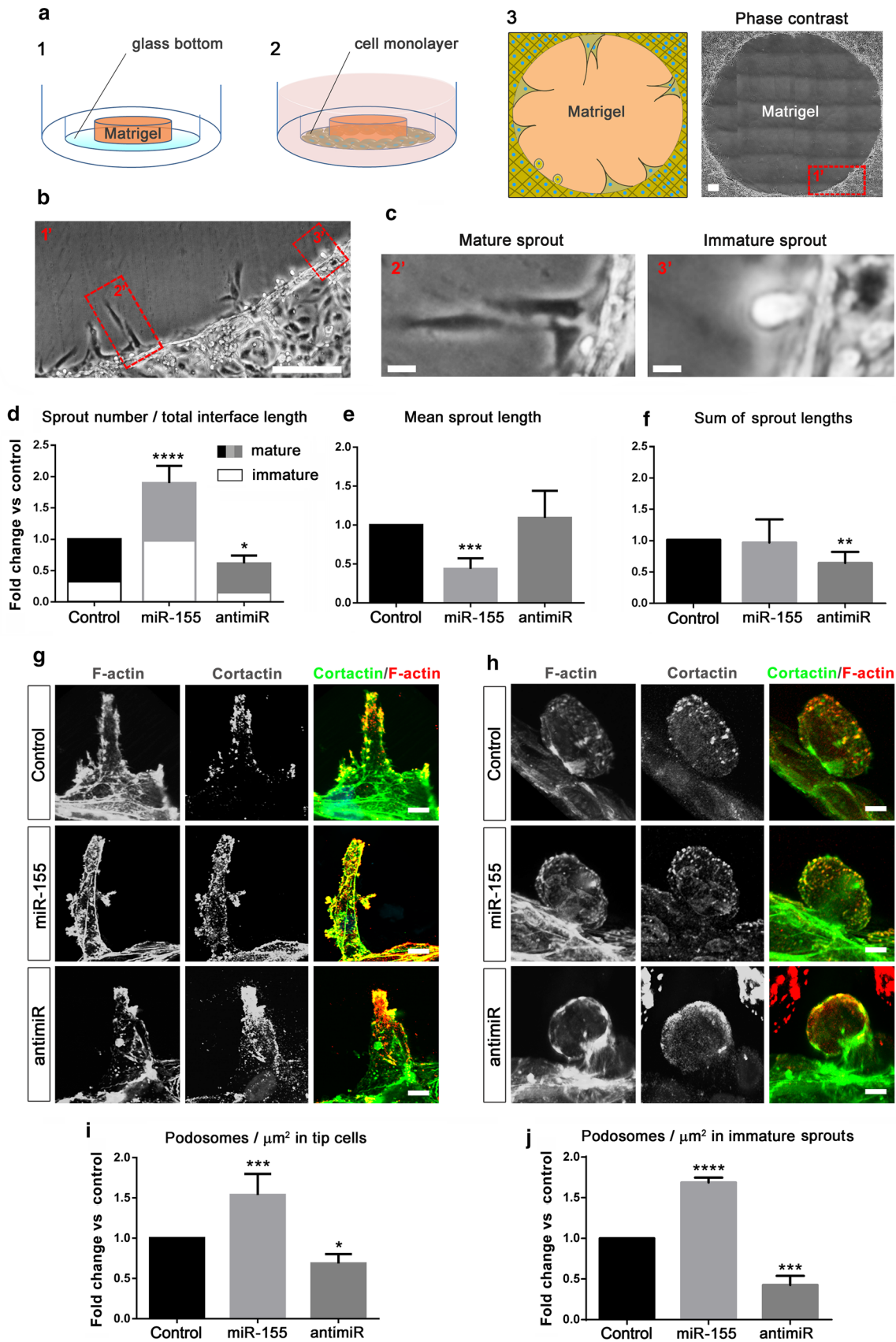
◀**Fig. 2** miR-155 regulates EC sprouting and podosome formation in vitro. **a** Cartoon showing the experimental setup of the invasion assay with the central Matrigel plug (1) around which ECs are seeded to form a monolayer (2). Sprouting ECs seen from the top; far-right image shows the ECs invading the plug by phase contrast (3). Scale bar: 400 µm. **b** Phase contrast images at higher magnification show the sprouts formed after 4 h. Scale bar: 50 µm. **c** High magnification images of the boxed regions in **b** showing the two types of sprouts, referred to as mature and immature sprouts. Scale bars: 10 µm. **d** Quantification of the number of angiogenic sprouts, mature and immature, in Si-control, miR-155 and antimiR-155-transfected ECs. $n = 5$ independent experiments, mean ± SD is shown. *$p < 0.05$, ****$p < 0.001$ vs Si-control, (one-way ANOVA Bonferroni multiple comparison test). **e**, **f** Quantification of the mean length and the sum of the lengths of angiogenic sprouts in Si-control, miR-155 and antimiR-155 transfected HMVECs. $n = 6$ independent experiments, mean ± SD is shown. **$p < 0.01$, ***$p < 0.001$, vs Si-control (one-way ANOVA Bonferroni multiple comparison test). **g**, **h** Stacked images (acquired with the confocal microscope) highlight the changes in podosome number in miR-155 and antimiR-155 transfected ECs. Scale bars: 5 µm. **i**, **j** Quantification of podosomes in 3D sprouts in Si-control, miR-155 and antimiR-155-transfected ECs. $n = 5$ and $n = 3$ independent experiments, mean ± SD is shown. *$p < 0.05$, **$p < 0.01$, ***$p < 0.001$, ****$p < 0.0001$, vs Si-control (one-way ANOVA Bonferroni multiple comparison test)

Extracellular matrix remodeling by podosomes relies on matrix proteases, of which the transmembrane metalloprotease MT1-MMP is the major enzyme. MT1-MMP is delivered via microtubules and exposed at podosome sites. Cells over-expressing miR-155 displayed brighter cell-surface MT1-MMP staining at podosome rosettes than control cells (Fig. 6a, b). This response was similar to that obtained upon VEGF-A stimulation. As expected, miR-155-induced podosome formation and associated matrix degradation were abolished in MT1-MMP-silenced cells (Fig. S5a, Fig. 6c, d). In the AIA (Fig. 2a), MT1-MMP colocalized with cortactin at 3D podosomes (Fig. S5b). Silencing MT1-MMP reduced miR-155-induced podosome formation in tip cell-like cells and sprouting capacities (Fig. 6e–g).

MT1-MMP also acts as a membrane-anchored activator, processing latent pro-MMP2 in complex with αVβ3 integrin into active MMP2 at the cell surface. We therefore analyzed MMP2 activity in cell supernatants by gelatin zymography. The secreted latent MMP2 proenzyme (which is activated by the assay) can be identified by its molecular mass at 72 kDa (pro-MMP9 (MW: 92 kDa) was not detected) (Fig. 7a). MMP2 was visualized by its gelatinase activity just below its precursor. A selective increase in MMP2 activity was observed with miR-155-transfected cells, whereas no change was detected in anti-miR155-transfected cells (Fig. 7b). miR-155 reduced MMP2 activity induced by VEGF-A stimulation. Taken together, these data show that miR-155 increases MMP2 activity while antimiR-155 has no significant effect. Therefore, the upregulation of MMP2 activity may have arisen from the processing of its precursor by MT1-MMP. Altogether, the results show that miR-155

regulates MT1-MMP in podosome formation and function, as does VEGF-A. However, beyond physiological levels, miR-155 impairs the EC response to VEGF-A.

miR-155 disturbs Notch signaling through Smad proteins

Like all miRs, miR-155 has multiple targets that regulate biological processes in a tissue type- and context-dependent manner [33]. We focused on Smad1 and Smad5, which are validated targets of miR-155 in aortic ECs [24]. In the latter cells, podosome formation is induced in response to TGF-β and potentiated by miR-155. BMP-Smad and Notch signaling pathways converge in ECs undergoing angiogenesis. Dll4-Notch and its crosstalk to VEGF balances the tip cell/stalk cell ratio [34]. As tip/stalk cell specification depends on the integration of Smad1/5 and Notch signaling cascades [8] [35, 36], we hypothesized that miR-155 could affect this pathway. Both Smad1 and Smad5 expression were reduced in miR-155-transfected cells, indicating that these proteins are also targets of this miR in HMVECs (Fig. 8a). Not unexpectedly, the phosphorylation of Smad1/5/8 diminished along with the expression of Smad1 and Smad5, so that changes in the expression of these transcription factors should globally result in an alteration of their signaling potential. Phospho-Smad1/5/8 was not modulated by VEGF (Fig. S6a, b). Silencing the expression of Smad1 and/or Smad5 phenocopied the characteristics of miR-155-enriched cells with respect to podosome formation and function (Fig. S7). Western blot experiments analyzing the cleavage of Notch intracellular domain (NICD) confirmed that Notch signaling was reduced in miR-155-transfected cells. In addition, induction of Dll4 and Jag1 in response to VEGF-A stimulation was significantly decreased. Nrp1, which allows tip cell formation by limiting Smad signaling [7], was downregulated (Fig. 8a). In contrast, inhibiting Notch signaling with DAPT did not affect Smad1 or Smad5 expression (Fig. S8). In vivo, we found that antimiR-155 enhanced Smad1/5 phosphorylation at the angiogenic front, suggesting the regulatory role of endogenous miR-155 on Smad1/5 during angiogenesis (Fig. 8b). In the remodeling plexus where Smad signaling is required for proper Notch signaling [8], Smad1/5 phosphorylation was impaired by miR-155 (Fig. 8c) in IB4-stained retinal vasculature. ERG1/2/3 EC nuclei staining confirmed that the Smad1/5 phosphorylation defect mainly affected ECs (Fig. S9). In addition, vascular permeability was increased (Fig. 8d). VE-cadherin staining confirmed that endothelial junctions were irregular, and thus most probably dysfunctional, in retinal vessels that had been exposed to miR-155 (Fig. 8e).

Collectively, these results show that miR-155 decreases Smad1/5 expression and Notch signaling and suggest that podosome induction is enabled through this pathway.
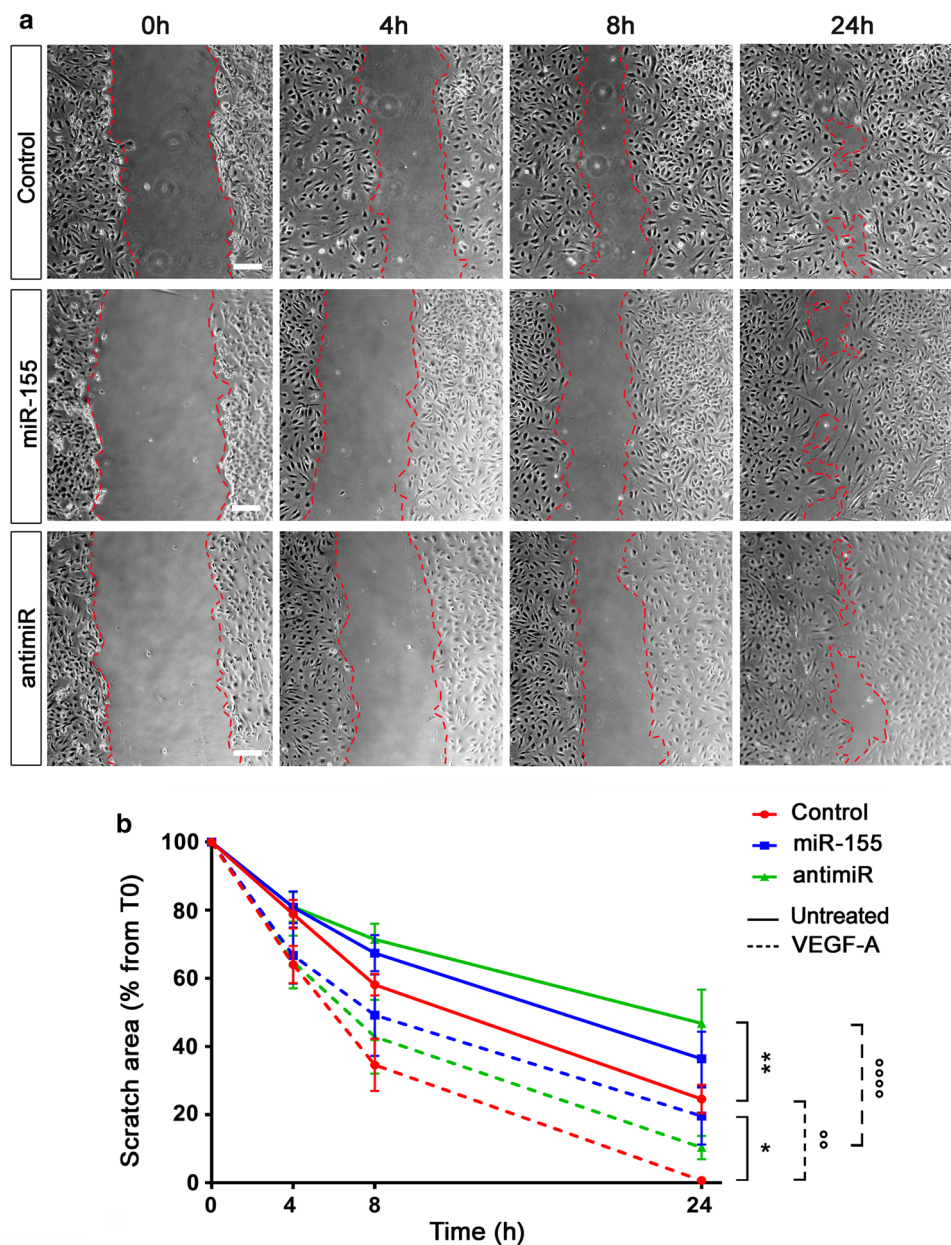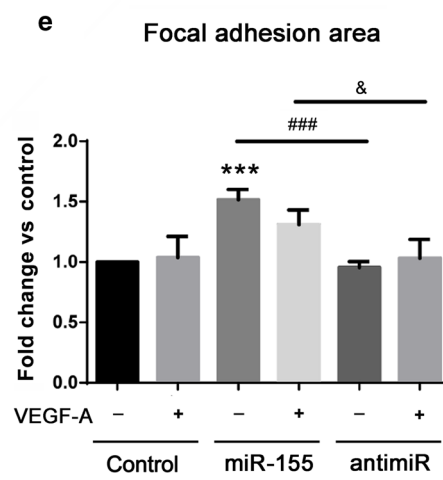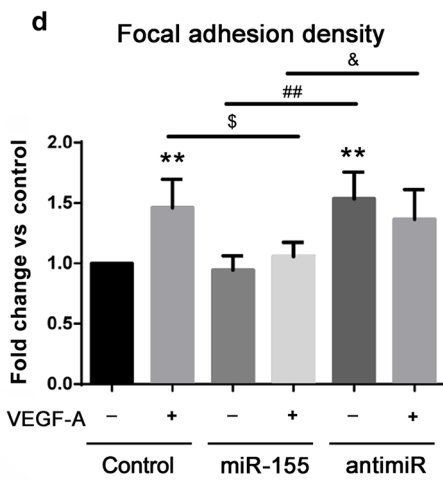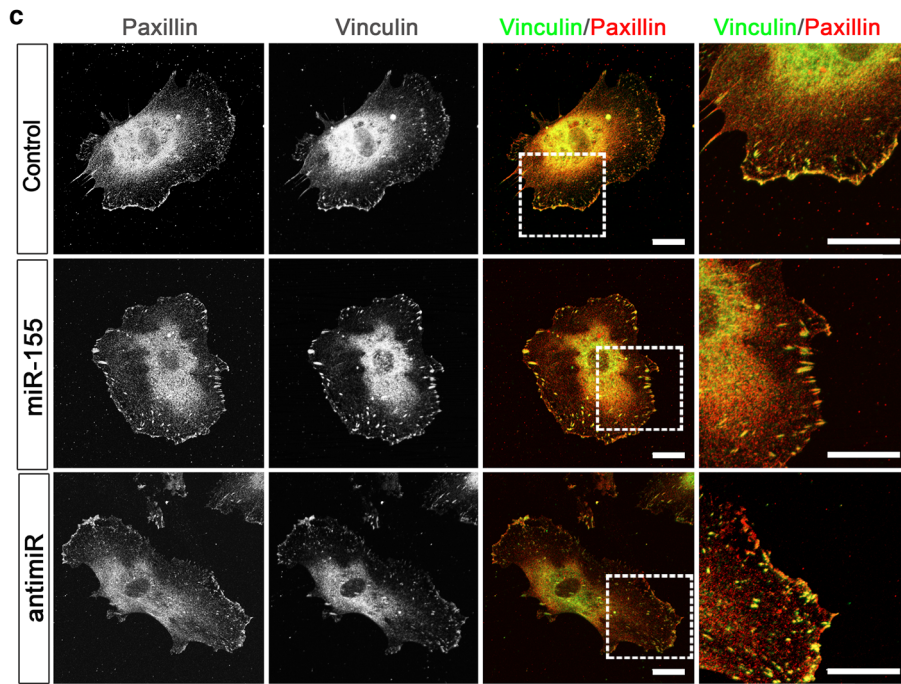
Fig. 3 Aberrant miR-155 levels in ECs affect their migration. **a** ECs were transfected with Si-control, miR-155 or antimiR-155 and seeded as a confluent monolayer in the presence or absence of VEGF-A. Representative phase-contrast images showing the wound at baseline (0 h) and 4 h, 8 h or 24 h after scraping the confluent monolayer cells (conditions without VEGF-A). Scale bars: 100 μm. **b** Quantification of the remaining gap area over time in the presence or absence of VEGF-A. $n = 4$ independent experiments performed in duplicate, mean $\pm$ SEM are shown. $*p < 0.05$, $**p < 0.01$ vs Si-control-transfected cells, $^{\circ\circ}p < 0.01$, $^{\circ\circ\circ\circ}p < 0.0001$ vs respective untreated cells (Two-way ANOVA followed by Bonferroni's multiple comparison test). **c** Representative images showing focal adhesion after vincu-lin/paxillin staining in ECs transfected with Si-control, miR-155 or antimiR-155. Scale bars: 10 μm. **d** Quantification of the number and **e** quantification of the average size of focal adhesions in ECs trans-fected with Si-control, miR-155 or antimiR-155, $n = 5$ independent experiments, mean $\pm$ SD is shown. $**p < 0.01$, $***p < 0.001$ vs untreated Si-control-transfected cells, $^{\$}p < 0.05$ vs VEGF-A-treated Si-control-transfected cells, $^{\#\#}p < 0.01$, $^{\#\#\#}p < 0.001$ vs untreated miR-155-transfected cells, $^{\&}p < 0.05$ vs VEGF-A-treated miR-155-trans-fected cells (two-way ANOVA Bonferroni multiple comparison test). **f** Table summarizing the total number and area of focal adhesions and the total cellular area measured in **d** and **e** in each experimental con-dition

Fig. 3 (continued)

miR-155 derived from tumor cells stimulates podosome formation in ECs

miR-155 is over-expressed in a variety of solid tumors and hematopoietic malignances and is therefore abundantly released in the microenvironment of cancer cells. Disruption of VEGF-induced angiogenesis in the retina model and alterations of EC phenotype by miR-155 suggest that miR-155 may underlie some aspects of pathological angiogenesis associated with malignancies. To investigate whether
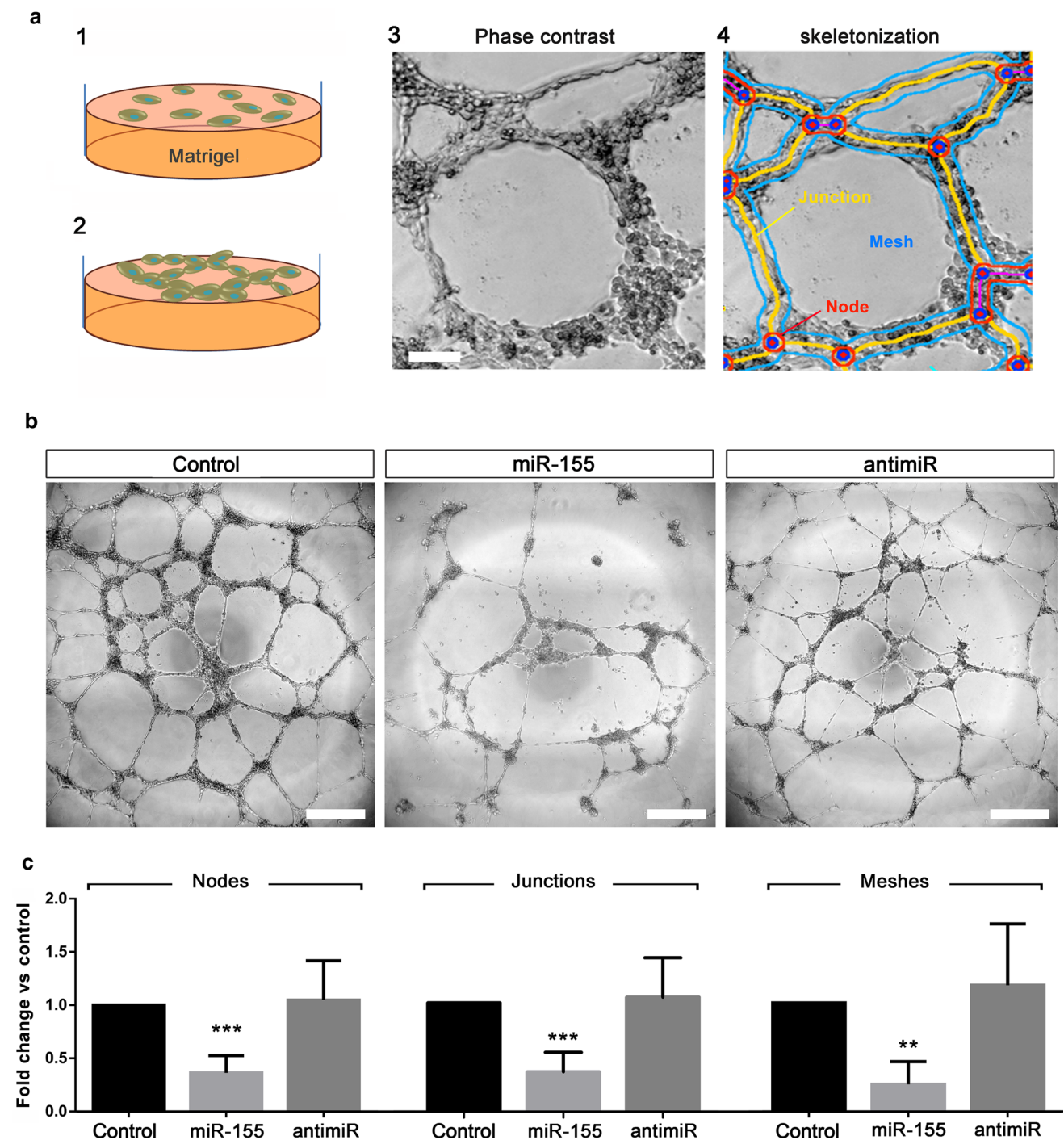
Fig. 4 Aberrant miR-155 levels in ECs affect tubulogenesis. **a** Cartoon showing the experimental setup consisting in seeding ECs on top of Matrigel (1) and undergoing morphogenesis (2). ECs undergo tubulogenesis (3) and junctions, meshes and nodes can be quantitated after skeletonization with ImageJ (4). Scale bar: 50 µm. **b** Representative images of tube formation by ECs transfected with Si-control, miR-155 or antimiR-155. Scale bars: 500 µm. **c** Quantification of nodes, junctions and meshes in the three conditions. $n=6$ independent experiments, mean$\pm$SD is shown. **$p<0.01$, ***$p<0.001$ vs Si-control-transfected cells (one-way ANOVA Bonferroni multiple comparison test)

miR-155-rich tumor cells influence EC phenotype and behavior, we first determined miR-155 expression in various tumor cell lines (Fig. S10a). For example, MDA-MB-231 breast tumor cells contain a higher copy number of miR-155 per cell than HMVECs (Fig. S10b). We then exposed HMVECs to these tumor cells in a co-culture system. In
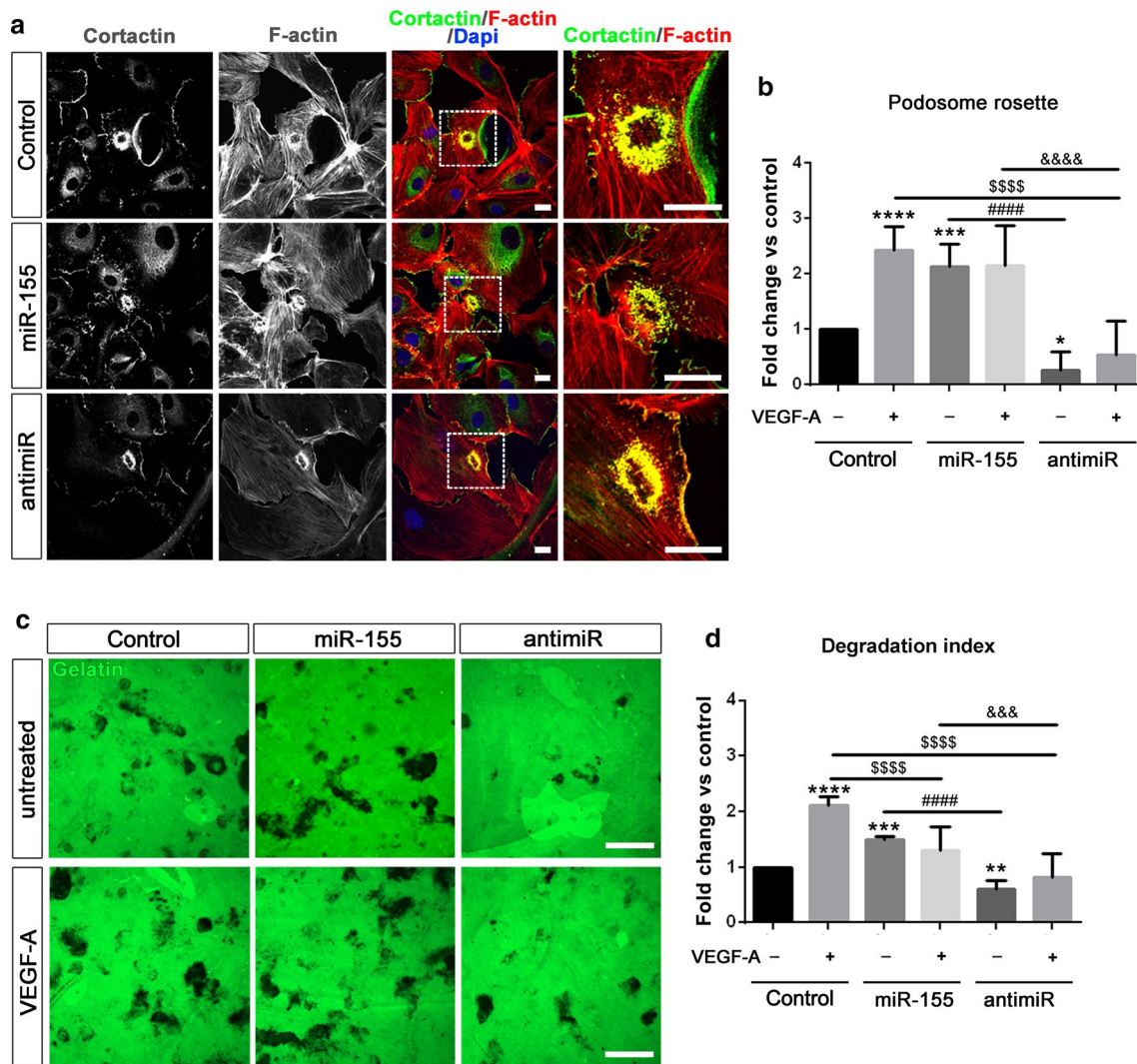
Fig. 5 miR-155 regulates the assembly and matrix-degrading potential of podosome rosettes in ECs. **a** Representative image of podosome rosettes in Si-control, miR-155 or antimiR-155-transfected ECs, visualized after double-staining for podosome markers (F-actin, cortactin). Scale bars: 10 μm. **b** Quantification of the podosome response in Si-control, miR-155 and antimiR-155-transfected cells, stimulated or not with VEGF-A. $n = 10$, mean ± SD is shown. *$p < 0.05$, ***$p < 0.001$, ****$p < 0.0001$ vs untreated Si-control-transfected cells. $^{\$\$\$\$}p < 0.0001$ vs VEGF-A-treated Si-control-transfected cells, $^{####}p < 0.0001$ vs untreated miR-155-transfected cells, $^{\&\&\&\&}p < 0.0001$ vs VEGF-A-treated miR-155-transfected cells (two-way ANOVA Bonferroni multiple comparison test). **c** Representative images of matrix degradation in Si-control, miR-155 or antimiR-155-transfected cells. Scale bars: 50 μm. **d** Quantification of gelatin degradation in Si-control, miR-155 or antimiR-155-transfected cells, stimulated or not with VEGF-A. $n = 11$, mean ± SD is shown. **$p < 0.01$, ***$p < 0.001$, ****$p < 0.0001$ vs untreated Si-control-transfected cells. $^{\$\$\$\$}p < 0.0001$ vs VEGF-A-treated Si-control-transfected cells, $^{####}p < 0.0001$ vs untreated miR-155-transfected cells, $^{\&\&\&}p < 0.001$ vs VEGF-A-treated miR-155-transfected cells (two-way ANOVA Bonferroni multiple comparison test)

these conditions, the number of podosome-forming ECs almost doubled (Fig. 9a). This effect was inhibited when HMVECs that had been transfected with antimiR-155 were used in the co-culture setup (Fig. 9b). Thus, a miR-155-rich environment promoted podosome formation and reducing cellular miR-155 levels impaired it.

Discussion

miR-155 is a typical multifunctional miRNA with distinct expression profiles. The targeted transcripts encode products such as receptors, kinases, DNA binding proteins and transcriptional regulatory proteins. These findings have led to the concept that miR-155 is a pleiotropic regulator of cell homeostasis. This is well illustrated in processes such as
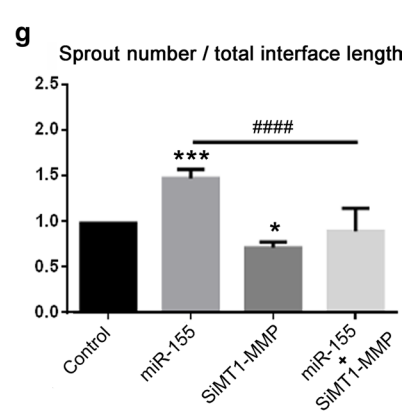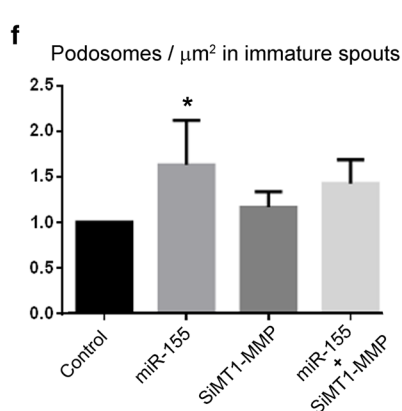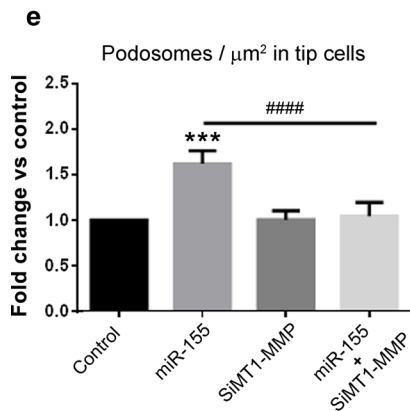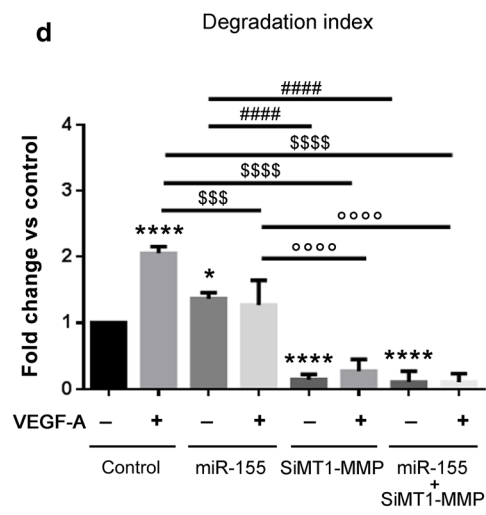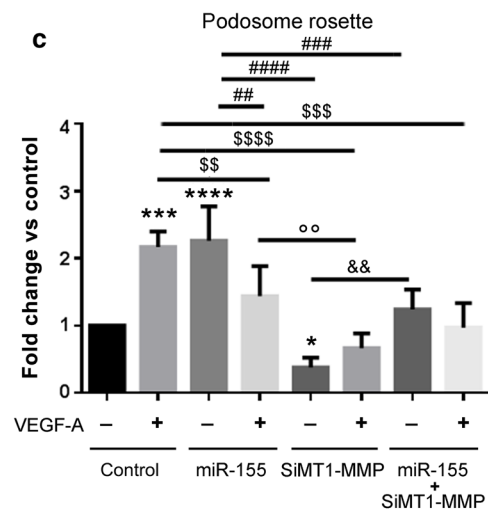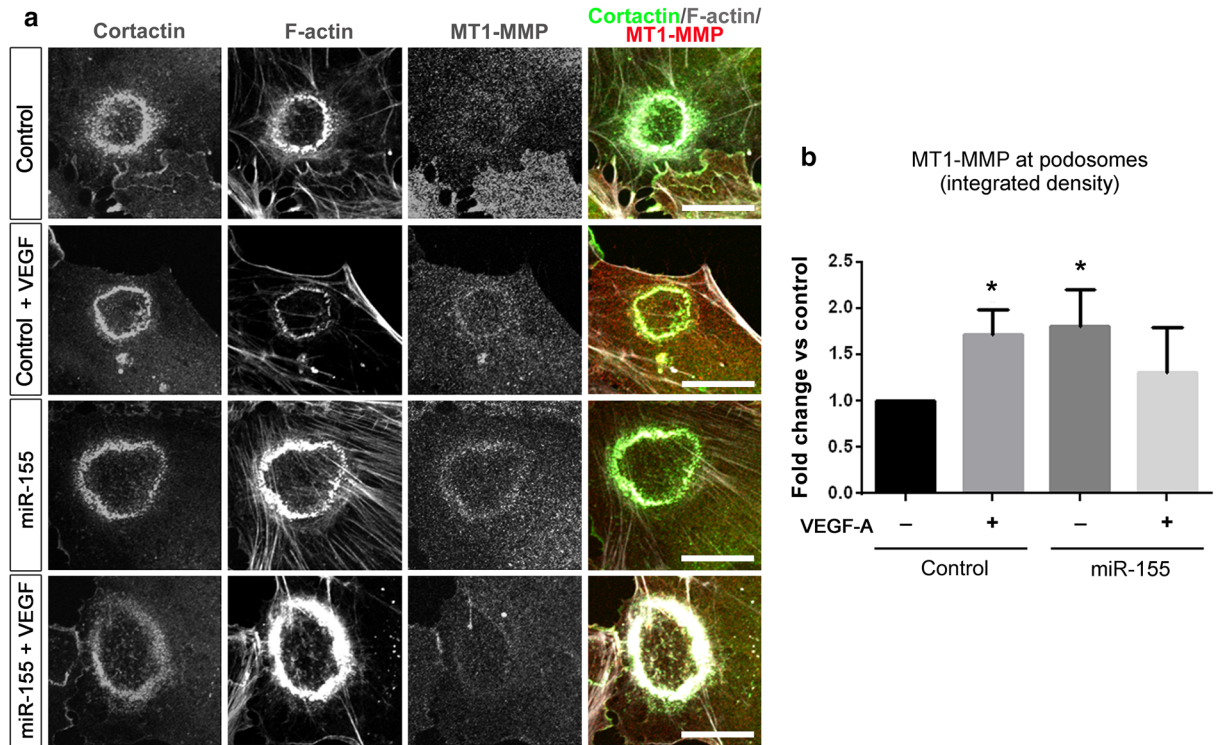
◀**Fig. 6** MT1-MMP regulates podosome proteolytic activities. **a** Representative images showing MT1-MMP exposed at podosome rosettes in non-permeabilized HMVECs, subsequently stained for F-actin and cortactin. Scale bars: 10 μm. **b** Quantification of MT1-MMP staining at podosomes. $n = 6$, mean $\pm$ SD is shown. $*p < 0.05$ vs untreated Si-control-transfected cells (one-way ANOVA Bonferroni multiple comparison test). **c** Quantification of podosome rosettes in ECs transfected with miR-155 or antimiR-155 in control or MT1-MMP silenced cells, stimulated or not with VEGF-A. **d** Quantification of matrix degradation in the same conditions as in **c** $n = 4$, mean $\pm$ SD is shown. $*p < 0.05$, $***p < 0.001$, $****p < 0.0001$ vs untreated Si-control-transfected cells. $^{\$\$}p < 0.01$, $^{\$\$\$}p < 0.001$, $^{\$\$\$\$}p < 0.0001$ vs VEGF-A-treated Si-control-transfected cells, $^{\#\#}p < 0.01$, $^{\#\#\#}p < 0.001$, $^{\#\#\#\#}p < 0.0001$ vs untreated miR-155-transfected cells, $^{\circ\circ}p < 0.01$, $^{\circ\circ\circ\circ}p < 0.0001$ vs VEGF-A-treated miR-155-transfected cells, $^{\&\&}p < 0.01$ vs untreated MT1-MMP silenced cells (two-way ANOVA Bonferroni multiple comparison test). **e, f** Quantification of podosomes in 3D mature sprouts (**e**), and immature sprouts (**f**) in response to miR-155 transfection in Si-control and Si-MMT1-MMP-transfected cells in AIAs. $n = 4$, mean $\pm$ SD is shown. $*p < 0.05$, $****p < 0.0001$, vs s Si-control-transfected cells, $^{\#\#\#\#}p < 0.0001$, vs miR-155-transfected cells (one-way ANOVA Bonferroni multiple comparison test). **g** Quantification of angiogenic (mature and immature) sprouts in the same conditions as **e** and **f**. $n = 5$, mean $\pm$ SD is shown. $*p < 0.05$, vs Si-control-transfected cells (one-way ANOVA Bonferroni multiple comparison test)

hematopoietic differentiation or modulation of the immune response [14, 37].

Our study reveals that miR-155 participates in physiological angiogenesis. The role of this miR in the process may have gone unnoticed until now because miR-155 is expressed at low levels in microvascular cells, and because its expression is not modulated by VEGF-A. In addition, most studies have used HUVECs (venous cells) as a model system, but these cells are not the ones that undergo angiogenesis under physiological conditions. We show here that endogenous physiological miR-155 ensures EC proteolytic capacities and migration that are essential for proper cell sprouting and invading capacities in response to VEGF-A. Altered VE-Cadherin, albumin extravasation and Col-IV staining in miR-155-exposed neovessels suggests that miR-155 also contributes to the dynamics and functionality of cell–cell junctions [38]. How miR-155 contributes to these processes remains to be established. Given the numerous targets of this miR (in silico analysis predicts hundreds of target genes and bioinformatic analyses indicates at least 11 angiogenesis-regulated genes [39]) and its presumed role in homeostasis, it is likely that different proteins are targeted, both directly and indirectly, at different stages of the process. The signals that control miR-155 endogenous levels in microvascular ECs in non-pathological conditions are not known. However, hemodynamic forces generated by blood flow and hypoxia, which play a role in angiogenesis, may be involved as these factors were shown to affect miR-155 expression in other cells [40, 41].

In sharp contrast, miR-155 has been extensively studied in pathological conditions. As in many cells, miR-155 is particularly responsive to inflammatory stimuli such as TNF-α, IL-1β, TGF-β and interferons in ECs [42], and the transcription factors NFkB and STATS (Signal Transducers and Activators of Transcription) are well known upstream regulators of miR-155. In addition, miRs operate not only as cell-autonomous modulators but also as paracrine ones through the release of EVs in the blood stream, in the regulation of cellular functions [43]. The fact that an unresolved inflammation process leads to aberrant angiogenesis suggested to us that miR-155 might be directly involved. In the same line, miR-155 is one of the most highly expressed miRs in cancer and its upregulation also promotes aberrant (tumor) angiogenesis [44].

To explore a possible link between miR-155 gain of function and angiogenesis, we investigated the consequences of exposing the growing vasculature of the retina to miR-155. The main defect was not increased angiogenesis but rather hypersprouting associated with increased podosome formation. Replication of this defect in cultured ECs showed that miR-155 directly affects EC properties. In vitro, miR-155 was sufficient to stimulate podosome formation, to upregulate MT1-MMP cell surface exposure and to increase MMP2 activity. However, cell migration was impaired in these cells. Thus miR-155 is likely to initiate EC sprouting by promoting podosome formation, but the process remains unproductive because these ECs are not invasive. We believe that invasion results from the combined effects of sprouting and migration. Thus, we can conceive that miR-155 affects ECs by increasing sprouting and reducing migration, with no net result on cell invasion.

Notwithstanding this, podosome proteolytic activities are expected to damage the BM in the mature vasculature and to compromise blood vessel integrity, as suggested by vascular leakage. Moreover, increased levels of miR-155 rendered ECs unable to respond to signals from VEGF-A. These findings may at least partly explain the defects in inflammatory and tumor vasculature.

Tip/stalk cell specification depends on the integration of Notch and Smad1/5 signaling cascades [35]. Based on the fact that (i) the phenotype in the miR-155-injected retina is reminiscent of that induced by impaired Notch signaling [5], (ii) inactivation of Smad1/5 results in impaired Dll4/Notch signaling [35], (iii) Smad1/5 repress the stalk cell phenotype [7] and (iv) Smad1/5 are known miR-155 targets [24], we could show that miR-155 reduced NICD generation in ECs exhibiting reduced Smad1/5 levels in vitro. We previously showed that lowering Notch signals in ECs is sufficient to enable podosome formation [9]. It thus appears that miR-155 could stimulate podosome formation by impairing Notch signaling through the downregulation of Smad1/5 expression. Supporting these conclusions, Smad1
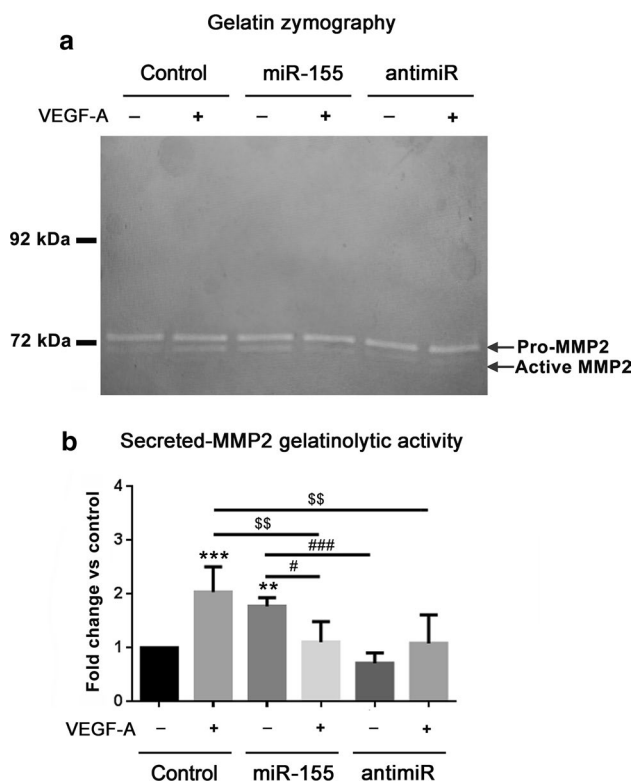
Fig. 7 miR-155-transfected ECs have increased MMP2 proteolytic activities. **a** Si-control and miR-155-transfected EC cultures were serum-starved for 1 day, then stimulated with VEGF-A or not for 24 h. Cell supernatants were collected and subjected to gelatinolytic analysis by in situ zymography. The bands corresponding to MMP2 precursor (pro-MMP2) and to active MMP2 are shown. **b** Quantification of active MMP2 in the six conditions by densitometry. $n = 7$ independent experiments, mean $\pm$ SD is shown. $**p < 0.01$, $***p < 0.001$, vs untreated Si-control-transfected cells, $^{\$\$}p < 0.01$, vs VEGF-A-treated Si-control-transfected cells, $^{\#}p < 0.05$, $^{\#\#\#}p < 0.001$ vs untreated miR155-transfected cells (two-way ANOVA Bonferroni multiple comparison test)

Fig. 8 miR-155 targets Smad1 and Smad5 in ECs and Notch signaling is altered. **a** ECs were transfected with Si-control, miR-155 or antimiR-155 oligonucleotides, then stimulated with VEGF-A or not for 24 h and cell extracts were prepared. Representative western blot experiments showing reduced Smad1, Smad5, Dll4 expression and NICD generation in miR-155-transfected cells, and reduced Jag1 and Nrp1 expression in response to VEGF-A stimulation in miR-155-transfected cells (left panels). Quantifications are shown (right panels). $n = 3$, mean $\pm$ SD is shown. $*p < 0.05$, $**p < 0.01$, $****p < 0.0001$ vs untreated Si-control-transfected cells. $^{\$}p < 0.05$, $^{\$\$}p < 0.01$, $^{\$\$\$}p < 0.001$ vs VEGF-A-treated Si-control-transfected cells, $^{\#}p < 0.05$, $^{\#\#}p < 0.01$, $^{\#\#\#}p < 0.001$ vs untreated miR-155-transfected cells, $^{\&}p < 0.05$, $^{\&}p < 0.01$, $^{\&\&\&}p < 0.001$ vs VEGF-A-treated miR-155-transfected cells (two-way ANOVA Bonferroni multiple comparison test). **b** Top panels: Representative images at the vascular angiogenic front of IB4 (green), phospho-Smad1/5/8 (red) and Hoechst (blue)-stained retinal whole-mounts from P6 mice intravitreally injected with the scrambled (Scr), miR-155 or antimiR-155 oligonucleotides at P4. Scale bars: 25 µm. Bottom panels: Black and white images showing inverted phospho-Smad 1/5/8 signals from the top panels. The quantifications of the number of phospho-Smad 1/5/8 and IB4 double positive cells, as well as the number of phospho-Smad 1/5/8 positive and IB4 negative cells, relative to the IB4 positive area are shown. **c** Same experimental setup as in **b** for the remodeling plexus. Graphs are presented as mean values $\pm$ SD (bars) and individual values (dots). A p-value less than 0.05 was considered as statistically significant (one-way ANOVA followed by Tukey's post-test) ($n = 6$ Scr-injected; $n = 6$ miR-155-injected; $n = 6$ antimiR-155-injected mice). Scale bars: 25 µm. **d**, **e** Exposure of the developing retinal vasculature to miR-155 compromises endothelial barrier function at the remodeling plexus. **d** Top panels: Representative images at the remodeling plexus of IB4 (green), albumin (red) and Hoechst (blue)-stained retinal whole-mounts from P6 mice intravitreally injected with the scrambled (Scr), miR-155 or antimiR-155 oligonucleotides at P4. Scale bar: 25 µm. Bottom panels: Black and white images showing inverted albumin signals from the top panels. The quantification of the albumin area per field is shown. Graphs are presented as mean values $\pm$ SD (bars) and individual values (dots). A p value less than 0.05 was considered as statistically significant (one-way ANOVA followed by Tukey's post-test) ($n = 6$ Scr- injected; 6 miR-155-injected; 6 antimiR-155-injected mice). **e** Representative images at the remodeling plexus of VE-cadherin (red) and Hoechst (blue)-stained retinal whole-mounts from P6 mice intravitreally injected with the scrambled (Scr), miR-155 or antimiR-155 oligonucleotides at P4. Scale bar: 25 µm. High magnification negative images from the three regions boxed in white show more irregular endothelial junctions in retinal vessels exposed to miR-155 compared to Scr and antimiR-155. (Images are representative for retinas from $n = 3$ Scr-injected; 3 miR-155-injected; 3 antimiR-155-injected mice)

or Smad5 silencing by an siRNA strategy phenocopied the effect of miR-155 on podosome formation and function. miR-155 over-expression also altered Nrp1 expression, which is required for the acquisition of the tip cell phenotype [7, 8], and this may account for the impaired induction of Dll4 and Jag1 in response to VEGF-A. Interestingly, low Notch activity is also sufficient to regulate MT1-MMP cell surface exposure [9]. These results reveal an unsuspected link between low Notch activity and proteolysis.

Inflammation and cancer are both associated with aberrant angiogenesis. Increased miR-155 is a common denominator of these pathological states [45]. miR-155 is also upregulated during aging [46] and likely involved in inflammaging (chronic inflammation in the absence of infection commonly observed during aging) [47]. Released into the bloodstream as extracellular vesicles [11] that can be endocytosed by ECs, miR-155 is expected to play a major role

in the angiogenic behavior of ECs in these diseases. Its deleterious effects have already been associated with cerebral stroke where miR-155 suppresses the expression of proteins related to tight junctions in the blood–brain barrier situated along blood vessels of the central nervous system [48].

miR-155 has also been studied in the context of pathological angiogenesis in mouse models. Most of them have used miR-155-deficient mice or strategies based on inhibition of miR-155 expression by antagomir [49]. In the oxygen-induced retinopathy (OIR) mouse model, miR-155 is consistently increased during all phases of the process, i.e., following hyperoxia at p12 (vaso-obliterative phase), and
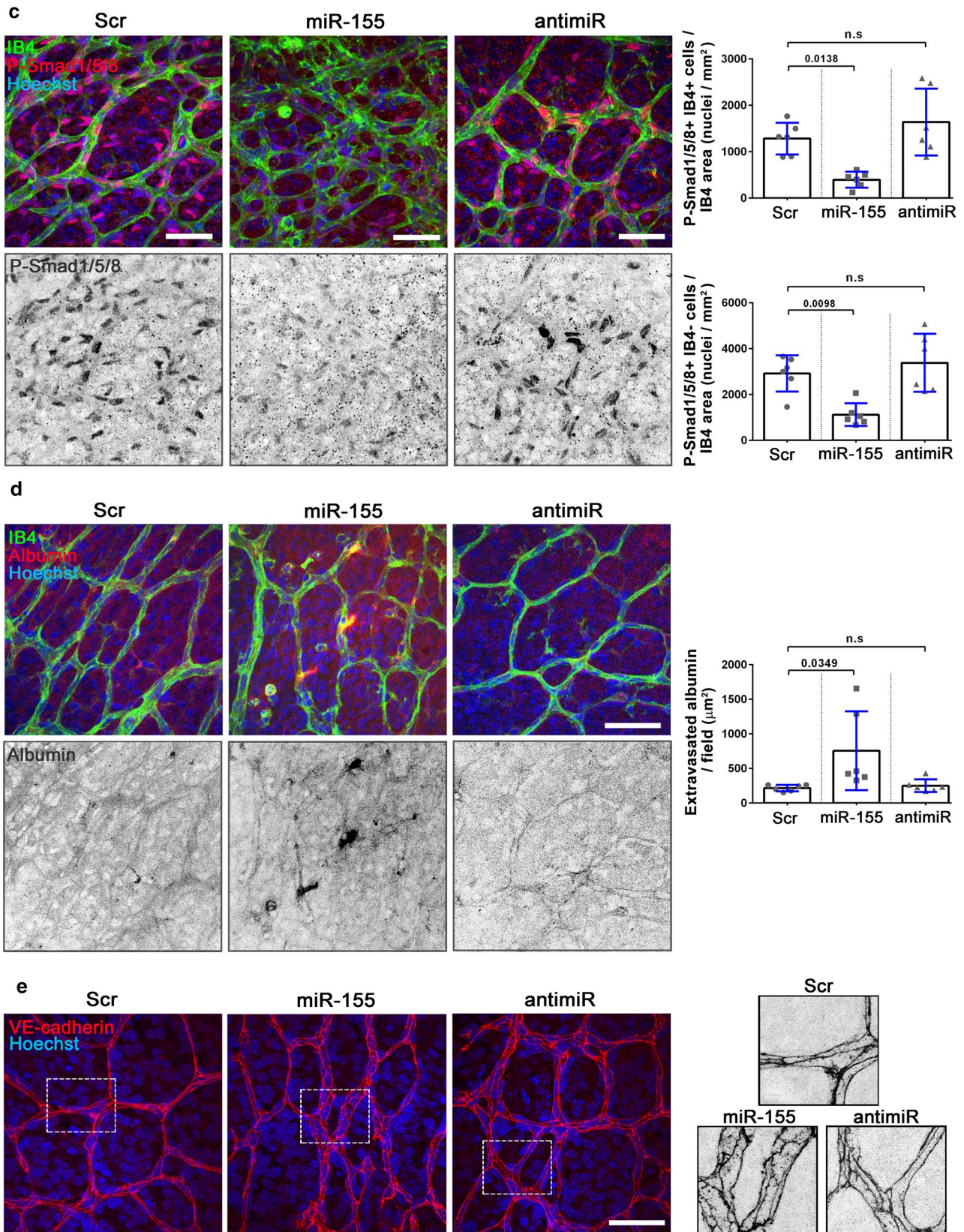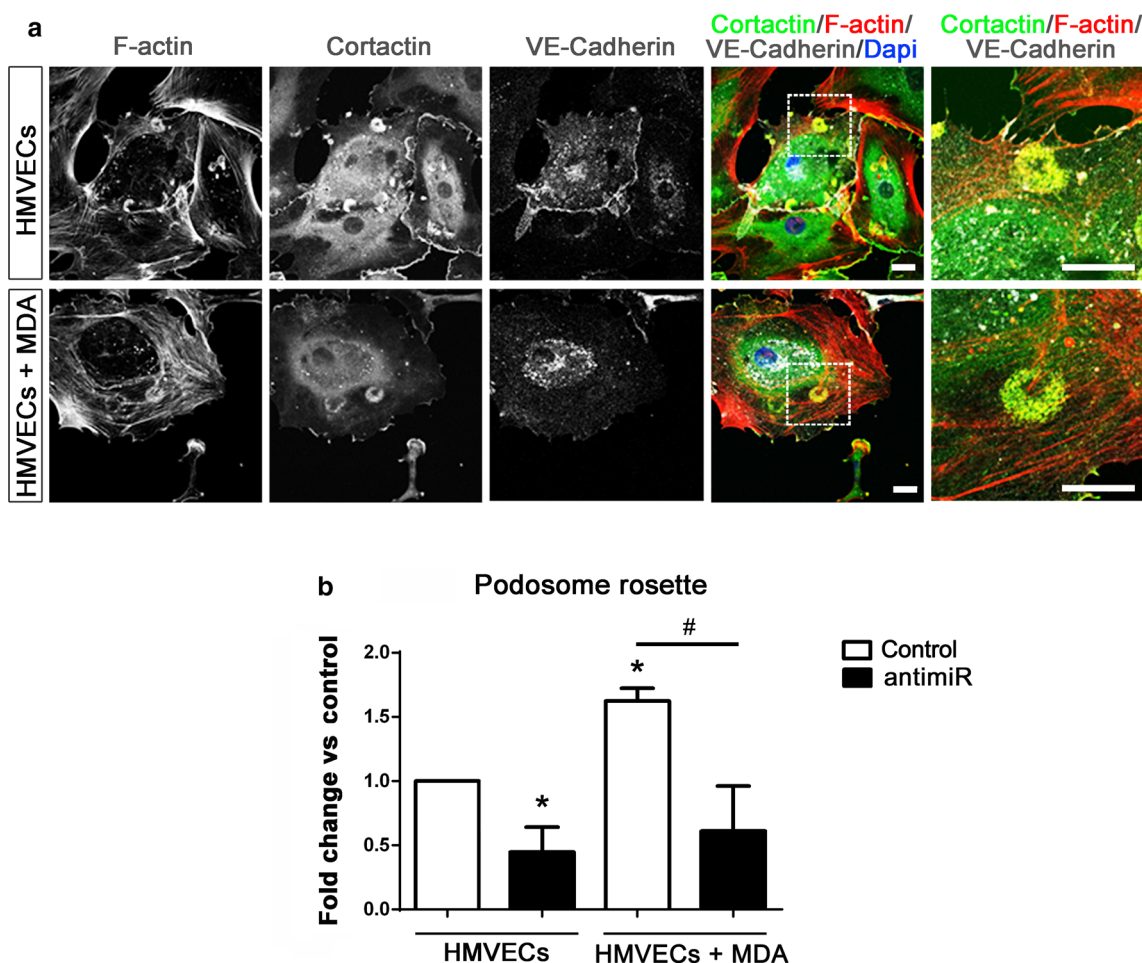
Remodeling plexus

Fig. 8 (continued)

Fig. 9 MDA-MB-231 cells stimulate podosome formation in ECs and this effect is neutralized when ECs are transfected with antimiR-155. **a** Representative images of podosome rosettes in ECs alone and in the ECs/MDAs co-cultures, identified by double-staining for podosome markers (F-actin/cortactin) in VE-Cadherin positive cells. Scale bars: 10 μm. **b** Quantification of podosome rosettes induced by co-culture with MDA-MB-231 cells in control or antimiR-155-transfected HMVECs. $n = 4$ independent experiments, mean ± SD is shown. *$p < 0.05$ vs Si-control-transfected EC monocultures, #$p < 0.05$, vs Si-control-transfected ECs + MDA cocultures (two-way ANOVA Bonferroni multiple comparison test)

ischemia at p17 (neovascularization phase). In this model, miR-155 deficiency prevents abnormal vessel growth, and allows normalization of the retinal vasculature after the ischemic insult. While these studies highlighted the involvement of miR-155 in a complex setting dominated by inflammation, the role of miR-155 was not investigated at the cellular and molecular levels.

An anti-miR-155 therapeutic tool, Cobomarsen (MRG-106), has been designed by Miragen Therapeutics and is already included in phase 2 clinical trials [50]. It consists in a chemically synthesized oligonucleotide with modifications to increase its bioavailability. It is presently the most advanced microRNA targeting pipeline [51, 52]. If miR-155 alters the integrity of the BM of mature vessels, the neutralization of its action by the administration of the miR-155 inhibitor should have beneficial effects at multiple levels: improved vessel homeostasis with decreased endothelial

permeability, restoration of mural cell coverage, restoration of EC quiescence, and restoration of beneficial interplay with immune cells. The beneficial effects of anti-miR-155 have already been reported on the vascular endothelium after ischemia [53]. The therapeutic advance would then be the restoration of both a functional vessel network and of an anatomical barrier. For cancer patients, this intervention is expected to improve perfusion of anti-tumor agents that is limiting in chemotherapies.

Several miRNAs have now been shown to regulate angiogenesis or EC functions. Let7-f, miR-27b, and miR-130a, miR-210, mir424 and the miR-17-92 cluster are known as pro-angiogenic miRNAs while the miR-221/222 family has opposite effects [54]. miR-155 can therefore be added to the list of miRNAs that regulate physiological and pathological angiogenesis.

Declarations

References

1. Sainson RC, Johnston DA, Chu HC, Holderfield MT, Nakatsu MN, Crampton SP et al (2008) TNF primes endothelial cells for angiogenic sprouting by inducing a tip cell phenotype. Blood 111(10):4997–5007. https://doi.org/10.1182/blood-2007-08-108597

2. Hellstrom M, Phng LK, Hofmann JJ, Wallgard E, Coultas L, Lindblom P et al (2007) Dll4 signalling through Notch1 regulates formation of tip cells during angiogenesis. Nature 445(7129):776–780. https://doi.org/10.1038/nature05571

3. Suchting S, Freitas C, le Noble F, Benedito R, Breant C, Duarte A et al (2007) The Notch ligand Delta-like 4 negatively regulates endothelial tip cell formation and vessel branching. Proc Natl Acad Sci USA 104(9):3225–3230. https://doi.org/10.1073/pnas.0611177104

4. Benedito R, Rocha SF, Woeste M, Zamykal M, Radtke F, Casanovas O et al (2012) Notch-dependent VEGFR3 upregulation allows angiogenesis without VEGF-VEGFR2 signalling. Nature 484(7392):110–114. https://doi.org/10.1038/nature10908

5. Benedito R, Roca C, Sorensen I, Adams S, Gossler A, Fruttiger M et al (2009) The notch ligands Dll4 and Jagged1 have opposing effects on angiogenesis. Cell 137(6):1124–1135. https://doi.org/10.1016/j.cell.2009.03.025

6. Hofmann JJ, Luisa I-A (2007) Notch expression patterns in the retina: an eye on receptor-ligand distribution during angiogenesis. Gene Expr Patterns 7(4):461–470. https://doi.org/10.1016/j.modgep.2006.11.002

7. Aspalter IM, Gordon E, Dubrac A, Ragab A, Narloch J, Vizan P et al (2015) Alk1 and Alk5 inhibition by Nrp1 controls vascular sprouting downstream of Notch. Nat Commun 6:7264. https://doi.org/10.1038/ncomms8264

8. Larrivee B, Prahst C, Gordon E, del Toro R, Mathivet T, Duarte A et al (2012) ALK1 signaling inhibits angiogenesis by cooperating with the Notch pathway. Dev Cell 22(3):489–500. https://doi.org/10.1016/j.devcel.2012.02.005

9. Spuul P, Daubon T, Pitter B, Alonso F, Fremaux I, Kramer I et al (2016) VEGF-A/Notch-induced podosomes proteolyse basement membrane collagen-IV during retinal sprouting angiogenesis. Cell Rep 17(2):484–500. https://doi.org/10.1016/j.celrep.2016.09.016

10. Conway EM (2021) VEGF-induced endothelial podosomes via ROCK2-dependent thrombomodulin expression initiate sprouting angiogenesis. Arterioscler Thromb Vasc Biol 41(5):1657–1671. https://doi.org/10.1161/ATVBAHA.121.315931

11. Daubon T, Spuul P, Alonso F, Fremaux I, Genot E (2016) VEGF-A stimulates podosome-mediated collagen-IV proteolysis in microvascular endothelial cells. J Cell Sci 129(13):2586–2598. https://doi.org/10.1242/jcs.186585

12. Veillat V, Spuul P, Daubon T, Egana I, Kramer I, Genot E (2015) Podosomes: multipurpose organelles? Int J Biochem Cell Biol 65:52–60. https://doi.org/10.1016/j.biocel.2015.05.020

13. Elton TS, Selemon H, Elton SM, Parinandi NL (2013) Regulation of the MIR155 host gene in physiological and pathological processes. Gene 532(1):1–12. https://doi.org/10.1016/j.gene.2012.12.009

14. Faraoni I, Antonetti FR, Cardone J, Bonmassar E (2009) miR-155 gene: a typical multifunctional microRNA. Biochim Biophys Acta 1792(6):497–505. https://doi.org/10.1016/j.bbadis.2009.02.013

15. Coumans FAW, Brisson AR, Buzas EI, Dignat-George F, Drees EEE, El-Andaloussi S et al (2017) Methodological guidelines to study extracellular vesicles. Circ Res 120(10):1632–1648. https://doi.org/10.1161/CIRCRESAHA.117.309417

16. Staszel T, Zapala B, Polus A, Sadakierska-Chudy A, Kiec-Wilk B, Stepien E et al (2011) Role of microRNAs in endothelial cell pathophysiology. Pol Arch Med Wewn 121(10):361–366

17. Urbich C, Kuehbacher A, Dimmeler S (2008) Role of microRNAs in vascular diseases, inflammation, and angiogenesis. Cardiovasc Res 79(4):581–588. https://doi.org/10.1093/cvr/cvn156

18. Riedl J, Flynn KC, Raducanu A, Gartner F, Beck G, Bosl M et al (2010) Lifeact mice for studying F-actin dynamics. Nat Methods 7(3):168–169

19. Haefliger JA, Allagnat F, Hamard L, Le Gal L, Meda P, Nardelli-Haefliger D et al (2017) Targeting Cx40 (Connexin40) expression or function reduces angiogenesis in the developing mouse retina. Arterioscler Thromb Vasc Biol 37(11):2136–2146. https://doi.org/10.1161/ATVBAHA.117.310072

20. Schneider CA, Rasband WS, Eliceiri KW (2012) NIH Image to ImageJ: 25 years of image analysis. Nat Methods 9:671–675

21. Tatin F, Grise F, Reuzeau E, Genot E, Moreau V (2010) Sodium fluoride induces podosome formation in endothelial cells. Biol Cell 102(9):489–498. https://doi.org/10.1042/BC20100030

22. Varon C, Tatin F, Moreau V, Van Obberghen-Schilling E, Fernandez-Sauze S, Reuzeau E et al (2006) Transforming growth factor beta induces rosettes of podosomes in primary aortic endothelial cells. Mol Cell Biol 26(9):3582–3594. https://doi.org/10.1128/MCB.26.9.3582-3594.2006

23. Le Roux-Goglin E, Varon C, Spuul P, Asencio C, Megraud F, Genot E (2012) Helicobacter infection induces podosome assembly in primary hepatocytes in vitro. Eur J Cell Biol 91(3):161–170. https://doi.org/10.1016/j.ejcb.2011.11.003

24. Curado F, Spuul P, Egana I, Rottiers P, Daubon T, Veillat V et al (2014) ALK5 and ALK1 play antagonistic roles in transforming growth factor beta-induced podosome formation in aortic endothelial cells. Mol Cell Biol 34(24):4389–4403. https://doi.org/10.1128/MCB.01026-14

25. Robertson B, Dalby AB, Karpilow J, Khvorova A, Leake D, Vermeulen A (2010) Specificity and functionality of

microRNA inhibitors. Silence 1(1):10. https://doi.org/10.1186/1758-907X-1-10

26. Varon C, Basoni C, Reuzeau E, Moreau V, Kramer IJ, Genot E (2006) TGFbeta1-induced aortic endothelial morphogenesis requires signaling by small GTPases Rac1 and RhoA. Exp Cell Res 312(18):3604–3619

27. Díaz B (2013) Invadopodia detection and gelatin degradation assay. Bio-Protoc 3(24):e997. https://doi.org/10.21769/BioProtoc.997

28. Tatin F, Varon C, Genot E, Moreau V (2006) A signalling cascade involving PKC, Src and Cdc42 regulates podosome assembly in cultured endothelial cells in response to phorbol ester. J Cell Sci 119(Pt 4):769–781

29. Stahl A, Connor KM, Sapieha P, Chen J, Dennison RJ, Krah NM et al (2010) The mouse retina as an angiogenesis model. Investig Ophthalmol Vis Sci 51(6):2813–2826. https://doi.org/10.1167/iovs.10-5176

30. Fraccaroli A, Franco CA, Rognoni E, Neto F, Rehberg M, Aszodi A et al (2012) Visualization of endothelial actin cytoskeleton in the mouse retina. PLoS One 7(10):e47488. https://doi.org/10.1371/journal.pone.0047488

31. Kim DH, Wirtz D (2013) Focal adhesion size uniquely predicts cell migration. FASEB J 27(4):1351–1361. https://doi.org/10.1096/fj.12-220160

32. Du P, Subbiah R, Park JH, Park K (2014) Vascular morphogenesis of human umbilical vein endothelial cells on cell-derived macromolecular matrix microenvironment. Tissue Eng Part A 20(17–18):2365–2377. https://doi.org/10.1089/ten.TEA.2013.0693

33. Hsin JP, Lu Y, Loeb GB, Leslie CS, Rudensky AY (2018) The effect of cellular context on miR-155-mediated gene regulation in four major immune cell types. Nat Immunol 19(10):1137–1145. https://doi.org/10.1038/s41590-018-0208-x

34. Beets K, Huylebroeck D, Moya IM, Umans L, Zwijsen A (2013) Robustness in angiogenesis: notch and BMP shaping waves. Trends Genet 29(3):140–149. https://doi.org/10.1016/j.tig.2012.11.008

35. Moya IM, Umans L, Maas E, Pereira PN, Beets K, Francis A et al (2012) Stalk cell phenotype depends on integration of Notch and Smad1/5 signaling cascades. Dev Cell 22(3):501–514. https://doi.org/10.1016/j.devcel.2012.01.007

36. Benn A, Alonso F, Mangelschots J, Genot E, Lox M, Zwijsen A (2020) BMP-SMAD1/5 signaling regulates retinal vascular development. Biomolecules 10(3):488. https://doi.org/10.3390/biom10030488

37. Mehta A, Baltimore D (2016) MicroRNAs as regulatory elements in immune system logic. Nat Rev Immunol 16(5):279–294. https://doi.org/10.1038/nri.2016.40

38. Neto F, Klaus-Bergmann A, Ong YT, Alt S, Vion AC, Szymborska JA et al (2018) YAP and TAZ regulate adherens junction dynamics and endothelial cell distribution during vascular development. Elife 7(e31037):1–30

39. Nariman-Saleh-Fam Z, Saadatian Z, Daraei A, Mansoori Y, Bastami M, Tavakkoli-Bazzaz J (2019) The intricate role of miR-155 in carcinogenesis: potential implications for esophageal cancer research. Biomark Med 13(2):147–159. https://doi.org/10.2217/bmm-2018-0127

40. Bruning U, Cerone L, Neufeld Z, Fitzpatrick SF, Cheong A, Scholz CC et al (2011) MicroRNA-155 promotes resolution of hypoxia-inducible factor 1alpha activity during prolonged hypoxia. Mol Cell Biol 31(19):4087–4096. https://doi.org/10.1128/MCB.01276-10

41. Weber M, Baker MB, Moore JP, Searles CD (2010) MiR-21 is induced in endothelial cells by shear stress and modulates apoptosis and eNOS activity. Biochem Biophys Res Commun 393(4):643–648. https://doi.org/10.1016/j.bbrc.2010.02.045

42. Mahesh G, Biswas R (2019) MicroRNA-155: a master regulator of inflammation. J Interferon Cytokine Res 39(6):321–330. https://doi.org/10.1089/jir.2018.0155

43. Chen X, Liang H, Zhang J, Zen K, Zhang CY (2012) Secreted microRNAs: a new form of intercellular communication. Trends Cell Biol 22(3):125–132. https://doi.org/10.1016/j.tcb.2011.12.001

44. Kong W, He L, Richards EJ, Challa S, Xu CX, Permuth-Wey J et al (2014) Upregulation of miRNA-155 promotes tumour angiogenesis by targeting VHL and is associated with poor prognosis and triple-negative breast cancer. Oncogene 33(6):679–689. https://doi.org/10.1038/onc.2012.636

45. Tili E, Croce CM, Michaille JJ (2009) miR-155: on the crosstalk between inflammation and cancer. Int Rev Immunol 28(5):264–284. https://doi.org/10.1080/08830180903093796

46. Sredni ST, Gadd S, Jafari N, Huang CC (2011) A parallel study of mRNA and microRNA profiling of peripheral blood in young adult women. Front Genet 2:49. https://doi.org/10.3389/fgene.2011.00049

47. Ekiz HA, Ramstead AG, Lee SH, Nelson MC, Bauer KM, Wallace JA et al (2020) T cell-expressed microRNA-155 reduces lifespan in a mouse model of age-related chronic inflammation. J Immunol 204(8):2064–2075. https://doi.org/10.4049/jimmunol.1901484

48. Lopez-Ramirez MA, Wu D, Pryce G, Simpson JE, Reijerkerk A, King-Robson J et al (2014) MicroRNA-155 negatively affects blood-brain barrier function during neuroinflammation. FASEB J 28(6):2551–2565. https://doi.org/10.1096/fj.13-248880

49. Yan L, Lee S, Lazzaro DR, Aranda J, Grant MB, Chaqour B (2015) Single and compound knock-outs of microRNA (miRNA)-155 and its angiogenic gene target CCN1 in mice alter vascular and neovascular growth in the retina via resident microglia. J Biol Chem 290(38):23264–23281. https://doi.org/10.1074/jbc.M115.646950

50. Rupaimoole R, Slack FJ (2017) MicroRNA therapeutics: towards a new era for the management of cancer and other diseases. Nat Rev Drug Discov 16(3):203–222. https://doi.org/10.1038/nrd.2016.246

51. Foss FM, Querfeld C, Kim HY, Pinter-Brown LC, William BM, Porcu P et al (2018) Phase 1 study of cobomarsen (MRG-106) in cutaneous T cell lymphoma and HTLV-1 associated T cell leukemia/lymphoma, ASCO Annual Meeting 2018, Abstract #2511

52. Querfeld C, Pacheco T, Foss F, Halwani A, Porcu P, Seto A et al (2016) Preliminary results of a phase 1 trial evaluating MRG-106, a synthetic microRNA antagonist (LNA antimiR) of microRNA-155, in patients with CTCL. Blood 128(22):1829. https://doi.org/10.1182/blood.V128.22.1829.1829

53. Caballero-Garrido E, Pena-Philippides JC, Lordkipanidze T, Bragin D, Yang Y, Erhardt EB et al (2015) In vivo inhibition of miR-155 promotes recovery after experimental mouse stroke. J Neurosci 35(36):12446–12464. https://doi.org/10.1523/JNEUROSCI.1641-15.2015

54. Chamorro-Jorganes A, Araldi E, Suarez Y (2013) MicroRNAs as pharmacological targets in endothelial cell function and dysfunction. Pharmacol Res 75:15–27. https://doi.org/10.1016/j.phrs.2013.04.002